Environmental conditions in the North Atlantic sector of the Arctic during the HALO–(AC)^3 campaign

Andreas Walbröl[1], Janosch Michaelis[2], Sebastian Becker[3], Henning Dorff[4], Irina Gorodetskaya[5,6], Benjamin Kirbus[3], Melanie Lauer[1], Nina Maherndl[3], Marion Maturilli[7], Johanna Mayer[8], Hanno Müller[3], Roel A. J. Neggers[1], Fiona M. Paulus[1], Johannes Röttenbacher[3], Janna E. Rückert[9], Imke Schirmacher[1], Nils Slättberg[7], André Ehrlich[3], Manfred Wendisch[3], and Susanne Crewell[1]

[1]Institute for Geophysics and Meteorology, University of Cologne, Cologne, Germany
[2]Alfred Wegener Institute, Helmholtz Center for Polar and Marine Research, Bremerhaven, Germany
[3]Leipzig Institute for Meteorology, Leipzig University, Leipzig, Germany
[4]Meteorological Institute of Hamburg, University of Hamburg, Hamburg, Germany
[5]Centre for Environmental and Marine Studies, University of Aveiro, Aveiro, Portugal
[6]Interdisciplinary Centre of Marine and Environmental Research (CIIMAR), University of Porto, Matosinhos, Portugal
[7]Alfred-Wegener-Institut, Helmholtz Center for Polar and Marine Research, Potsdam, Germany
[8]German Aerospace Centre (Deutsches Zentrum für Luft- und Raumfahrt (DLR)), Oberpfaffenhofen, Germany
[9]Institute of Environmental Physics, University of Bremen, Bremen, Germany

Correspondence: Andreas Walbröl (a.walbroel@uni-koeln.de)

Abstract.

Centered around the High Altitude and Long Range (HALO) research aircraft and the collaborative research project on Arctic Amplification (AC)^3, the airborne field campaign HALO–(AC)^3 took place from 07 March to 12 April 2022. Its major goal was to observe the transformation of air masses during their meridional transport in the North Atlantic sector of the Arctic. We evaluate the meteorological and sea ice conditions during the campaign based on the European Centre for Medium–Range Weather Forecasts (ECMWF) Reanalysis v5 (ERA5), satellite data, and atmospheric soundings with respect to climatology. HALO–(AC)^3 started with a warm period (11–20 March) where strong southerly winds prevailed that caused moist and warm air intrusions (MWAIs). Two MWAIs were detected as Atmospheric Rivers (ARs). Compared to the ERA5 climatology (1979–2022), record breaking vertically integrated poleward heat and moisture fluxes averaged over the Fram Strait latitudes were found. These warm and moist air masses caused the highest rainfall rates over the sea ice northwest of Svalbard since the beginning of the ERA5 climatology. During the subsequent cold period, starting after the passage of a strong cyclone on 21 March, northerly winds advected colder air into the Fram Strait. Marine cold air outbreaks (MCAOs) prevailed until 08 April, interrupted by short periods of aged subpolar warm air. On average, the entire campaign period was warmer than the climatological mean due to the strong influence of the ARs. In the Fram Strait, the sea ice concentration (SIC) was well within the climatological variability, staying within the 10–90th percentiles over the entire campaign duration. However, during the warm period, an atypically large polynya opened north of Svalbard. For potential future studies, we describe the environmental conditions of the most significant weather events (ARs, MCAOs, Polar Low, and Arctic cirrus) during HALO–(AC)^3 in detail. Comparing atmospheric conditions over the Fram Strait with Ny–Ålesund (Svalbard), temporal shifts up to one day have been identified. The temporal shift and orographic effects must be taken into account when combining airborne HALO–(AC)^3

20   measurements with ground based observations at Ny–Ålesund. Compared to previous airborne field campaigns focusing on the evolution of (mixed–phase) clouds, a larger variety of MCAO conditions were observed during HALO–(AC)[3]. Our study may serve as basis for future analyses of the data collected during the campaign.

1 Introduction

The Arctic experiences a drastic temperature increase almost 4 times stronger compared to the rest of the globe (Rantanen et al.,
2022). This enhanced warming is known as Arctic Amplification and is caused by several feedback mechanisms (Serreze et al.,
2009; Screen and Simmonds, 2010; Serreze and Barry, 2011). While the contribution of some feedback mechanisms to Arctic
Amplification can be regarded as scientific consensus (e.g., sea ice–albedo feedback, Serreze et al., 2009), others are not yet
sufficiently explored and their contribution is uncertain (e.g., influence of clouds, lapse rate feedback, linkages between Arctic
and mid–latitudes, Wendisch et al., 2023). As the Arctic warms faster than the mid–latitudes, the meridional temperature
gradient decreases in most heights of the troposphere, likely resulting in a weaker jet stream and possibly enhancing the
tendency to meander (Francis and Vavrus, 2015). A more meandering jet would result in an increasing number of poleward
moist and warm air intrusions (MWAIs) and southward cold air outbreaks (CAOs). However, the tropical upper troposphere
warms while the Arctic lower stratosphere cools, enhancing meridional temperature gradients at higher altitudes (Lee et al.,
2019; Stendel et al., 2021). The frequency of meridional transport through the North Atlantic has increased during the last
decades while it stayed constant or even decreased in other regions (Mewes and Jacobi, 2019). You et al. (2022) found a
positive trend in the frequency and duration of atmospheric blocking over the Barents Sea especially in winter, supporting the
statement of an enhanced North Atlantic pathway for meridional transport.

MWAIs frequently transport large amounts of heat and moisture into the Arctic through the Atlantic sector (Woods and
Caballero, 2016). When the warm air is pushed upwards over cold Arctic air masses, deep cloud systems including mixed–
phase clouds may form. During MWAIs, cirrus clouds, whose radiative effect is not well explored over sea ice (Hong and
Liu, 2015; Marsing et al., 2023), can be formed or advected to the Arctic. Woods et al. (2013) and Woods and Caballero
(2016) stress that intense MWAIs have a large effect on the downward terrestrial radiation at the surface, contributing to the
warming of the Arctic. Such MWAIs precondition the sea ice for the melting season, resulting in lower sea ice extent at the
end of the summer (Kapsch et al., 2013, 2019). Numerical models still struggle to accurately represent the mixed–phase clouds
and the transformation processes of the air masses (Pithan et al., 2014; Cohen et al., 2020). MWAIs can often be linked with
filamentary bands of strong moisture transport, known as Atmospheric Rivers (ARs, Newell et al., 1992). ARs are responsible
for over $90\,\%$ of the poleward moisture transport across the mid–latitudes and are frequently accompanied by strong winds and
precipitation (Nash et al., 2018). While the precipitation can cause snow accumulation during ARs in the Arctic, the enhanced
emission of downward terrestrial radiation by the clouds can lead to melting of snow and sea ice (Neff et al., 2014; Komatsu
et al., 2018; Mattingly et al., 2018, 2020; Bresson et al., 2022; Viceto et al., 2022). In a warming climate, ARs are expected to
shift polewards and intensify due to the increased moisture load (Ma et al., 2020).

CAOs are often responsible for severe weather events in the high– and mid–latitudes and mainly occur in winter and spring
(Fletcher et al., 2016; Pithan et al., 2018). Here, we focus on marine CAOs (MCAOs) where cold and dry air is advected
southwards from the sea ice to the ice–free (open) ocean. Over the open ocean, the strong temperature contrast between the
surface and the lower tropospheric air leads to intense fluxes of sensible and latent heat, responsible for $60–80\,\%$ of the oceanic
heat losses in that region (Papritz and Spengler, 2017). This heat and moisture transfer into the atmosphere destabilizes the

boundary layer and leads to the formation of cloud streets, which later develop into open cells. This cloud evolution is not well represented in models but an important feature (Pithan et al., 2018). MCAOs can also cause the formation of Arctic mesoscale cyclones (Polar Lows, Rasmussen and Turner, 2003; Zahn and von Storch, 2008), which may locally lead to heavy precipitation and strong winds. The formation processes of Polar Lows and their relation to MCAOs are still not fully understood, partly due to the sparsity of measurements in the Arctic (Moreno-Ibáñez et al., 2021).

So far, observations of air mass transformations in the Arctic have mostly been conducted from a fixed local position (Eulerian view). Only a few aircraft based samplings of air mass properties over a limited regional area have been reported (e.g., Wendisch et al., 2019; Mech et al., 2022). To observe air mass transformation processes along their meridional pathway in a Eulerian view, multiple stations that are aligned with the wind direction would be needed. Therefore, Pithan et al. (2018) proposed a quasi–Lagrange approach following air masses to and from the Arctic, which motivated the field campaign HALO–(AC)[3] within the Transregional Collaborative Research Center TRR 172 (TRR 172) "Arctic Amplification: Climate Relevant Atmospheric and Surface Processes and Feedback Mechanisms (AC)[3]". The campaign was designed to obtain quasi–Lagrange observational data of air mass transformations during MWAIs and MCAOs to gain process understanding and evaluate the performance of weather and climate models (Wendisch et al., 2021).

During HALO–(AC)[3], extensive remote sensing and in situ measurements of surface, cloud and thermodynamic properties have been performed between the Norwegian Sea and the North Pole from 11 March to 12 April 2022 with three research aircraft (HALO, Polar 5, and Polar 6). The High Altitude and LOng-range research aircraft (HALO) operated by the German Aerospace Center (DLR, Ziereis and Gläßer, 2006; Stevens et al., 2019) is a modified Gulfstream G550, which has a sufficient operating range (9000 km in altitudes up to 15 km) for quasi–Lagrange air mass observations and was based in Kiruna during HALO–(AC)[3]. For HALO–(AC)[3], it was equipped with a similar instrumental payload as during the EUREC4A campaign (Stevens et al., 2019; Konow et al., 2021). Polar 5 and Polar 6 (P5 and P6) were based in Longyearbyen and operated by the Alfred Wegener Institute, Helmholtz Centre for Polar and Marine Research (AWI, Wesche et al., 2016) in a similar coordinated way as during the ACLOUD campaign (Wendisch et al., 2019).

This study focuses on the environmental conditions during HALO–(AC)[3] and their climatological context to serve as comprehensive reference in future studies. After introducing the data basis and methods in Sect. 2, we describe the synoptic development during two dominating periods in Sect. 3.1. We also provide a view on the conditions at Ny–Ålesund (Sect. 3.2), where future studies will use the extensive measurements from the French–German Atmospheric Observatory AWIPEV. Sea ice conditions in the North Atlantic sector of the Arctic are presented in Sect. 3.3. We further analyse the origin and strength of the MWAIs and ARs (Sect. 4.1), the conditions during the MCAO periods (Sect. 4.2), the formation and environmental characteristics of the Polar Low (Sect. 4.3), and Arctic cirrus clouds (Sect. 4.4), before concluding our study in Sect. 5.

2 Data and Methods

2.1 Study domain

HALO–(AC)[3] flight tracks cover the North Atlantic sector of the Arctic, the major pathway of MWAIs (Johansson et al., 2017;
You et al., 2022). Based on the flight tracks, we selected three domains for our synoptic analysis as shown in Fig. 1. The exact
geographical coordinates of the domains are listed in Appendix A, Table A1. From north to south the domains are referred
to as northern region (central Arctic north of Svalbard and Greenland), central region (Fram Strait and Greenland Sea), and
southern region (Greenland and Norwegian Seas between Svalbard and Norway). A particular focus lies on the central region,
where measurements were performed with all three aircraft.

2.2 Atmospheric conditions observed from HALO and at Ny–Ålesund

Vertical profiles of temperature, relative humidity, pressure and wind were recorded with RD94 dropsondes launched from
HALO (Hock and Franklin, 1999; George et al., 2021) and radiosondes launched at the Atmospheric Observatory of the
French–German AWIPEV research base in Ny–Ålesund (Svalbard) every 6 hours (Vaisala RS41, Maturilli, 2020b). From the
radiosonde profiles, we identified the thermal tropopause according to the WMO definition as the lowest level at which the
temperature lapse rate falls below $2\,\mathrm{K\,km^{-1}}$ and does not exceed this value for the next $2\,\mathrm{km}$. The integrated water vapour
(IWV) was calculated from profiles of air pressure and specific humidity, which was derived from the temperature and relative
humidity measurements. Ground based meteorological measurements gathered at AWIPEV provide an additional view on the
environmental conditions during HALO–(AC)[3] in the central region (Maturilli et al., 2013; Maturilli, 2020a). Additionally,
we used data from the CL–51 ceilometer to assess the cloud conditions at Ny–Ålesund (Maturilli and Ebell, 2018; Maturilli,
2022).

2.3 Satellite observations of sea ice

We focused on sea ice concentration (SIC), i.e., the percentage of a satellite pixel (grid cell in ERA5) covered by sea ice, derived
from satellite measurements to describe the sea ice conditions during HALO–(AC)[3]. In general, we separated observations for
areas with and without sea ice (latter is also termed open water) through the threshold of $15\,\%$ SIC. Satellite based passive
microwave radiometers provide a long–term observation of sea ice (Spreen and Kern, 2016). Here, we used the OSI SAF
Global Sea Ice Concentration Climate Data Record (SIC CDR v2.0), namely the product OSI–450 from 1979 to 2015, and the
complementary Interim Climate Data Record OSI–430–b from 2016 onwards (OSI SAF, 2017; Copernicus Climate Change
Service (C3S), 2020). The product is based on low–frequency passive microwave satellite data and is described in Lavergne
et al. (2019). The datasets are available daily with a grid spacing of $25\,\mathrm{km} \times 25\,\mathrm{km}$.

To study the evolution of SIC during HALO–(AC)[3] at a higher spatial resolution, we used the merged MODIS–AMSR2 SIC
dataset, available daily at $1\,\mathrm{km}$ resolution. The merged MODIS–AMSR2 product (Ludwig et al., 2020) takes advantage of the
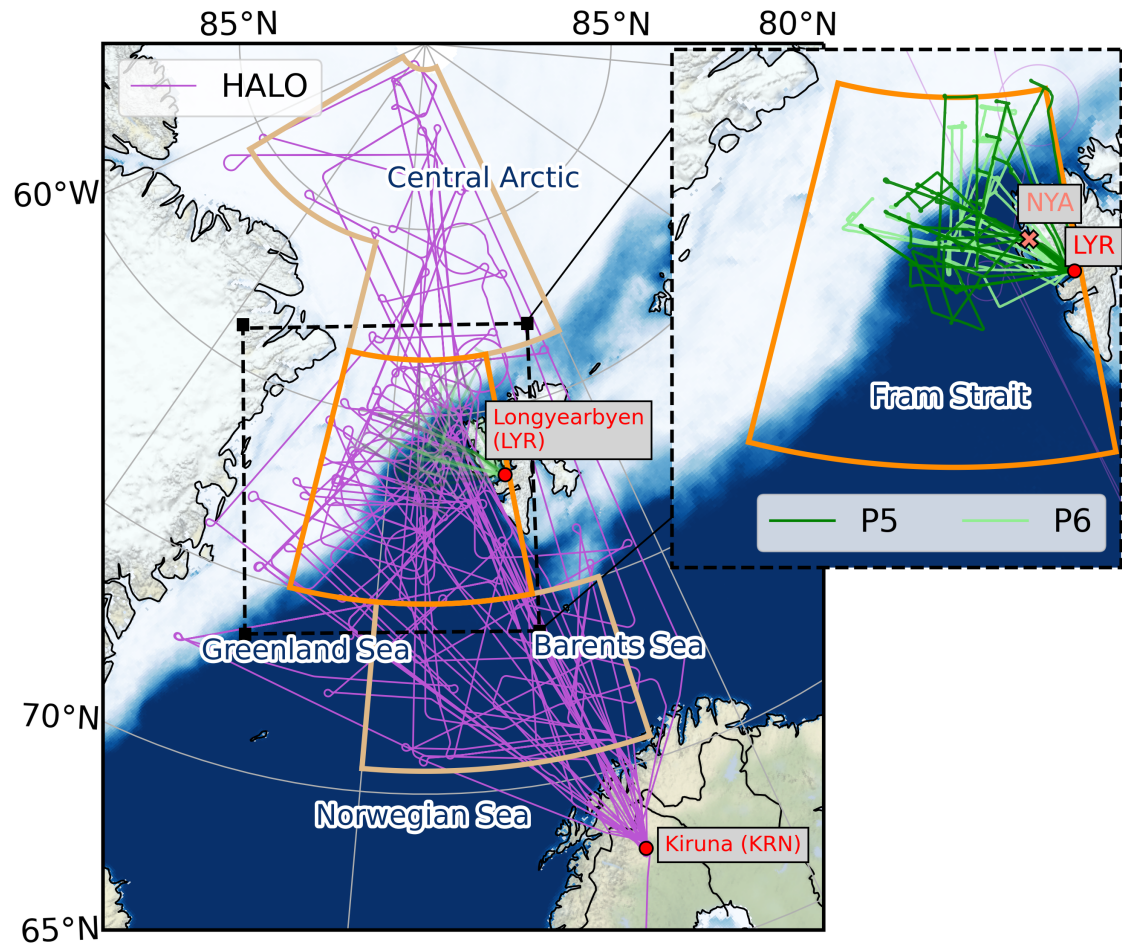
Figure 1. Flight tracks of HALO (purple), as well as P5 and P6 (dark and light green, zoomed domain in the right panel) during HALO–$(AC)^3$. For orientation, the mean sea ice concentration from 07 March to 12 April 2022 based on AMSR2 satellite data (Spreen et al., 2008) is showed as filled contours. The three measurement domains (southern region, central region, and northern region) are marked as yellow and orange boxes. The central region is highlighted. The orange label NYA in the zoomed domain marks the location of Ny–Ålesund.

high spatial resolution of thermal infrared (Drüe and Heinemann, 2004), and of the independence of cloud cover of microwaves (Spreen et al., 2008).

2.4 Reanalysis data

120 To analyse the weather development, we used the ERA5 reanalysis from the European Centre for Medium–Range Weather Forecasts (ECMWF). ERA5 offers hourly data output since 1950 with a horizontal resolution of 31 km and 137 vertical model levels (Hersbach et al., 2018a, b, 2020). ERA5 represents clouds and precipitation in the Arctic better than other reanalyses

(Graham et al., 2019a; Avila-Diaz et al., 2021). Additionally, ERA5 features a higher vertical resolution than other reanalyses, which leads to more accurate wind fields and, thus, to improved water vapour transport estimates (Graham et al., 2019b).

However, ERA5 shows higher warm biases over sea ice of near surface temperatures than other reanalyses due to the misrepresentation of the stable stratification (Wang et al., 2019; Yu et al., 2021). During HALO–(AC)[3], dropsonde measurements launched from HALO were assimilated into ERA5. The climatological comparisons presented here are based on the years 1979–2022 unless specified differently. Grid points with a land fraction > 0 have been excluded from our analysis according to the ERA5 land–sea–mask. Domain averages of the regularly gridded ERA5 quantities were calculated as area averages weighted by the cosine of the latitude to respect the increasing data point density with increasing latitudes. In the following, we describe the processing of ERA5 data and derivation of indices calculated for our analysis.

2.4.1 Detection of Atmospheric Rivers and moist and warm air intrusions

Woods and Caballero (2016) detect moist air intrusions into the Arctic when the vertically integrated meridional moisture flux ($\text{IVT}_{\text{north}}$) at 70° N exceeds $200\,\text{Tg}\,\text{d}^{-1}\,\text{deg}^{-1}$ ($60.6\,\text{kg}\,\text{m}^{-1}\,\text{s}^{-1}$) over a duration of at least 1.5 days and a zonal extent of at least 9°. For our purpose, we adapted this detection and defined MWAIs with positive daily means of $\text{IVT}_{\text{north}}$ averaged over the central region. An MWAI is considered weak (strong) when $\text{IVT}_{\text{north}}$ is below (equal or above) $100\,\text{kg}\,\text{m}^{-1}\,\text{s}^{-1}$. Additionally, we computed the temporal mean, 25–75th and 10–90th percentiles over the climatology period. In this study, ARs were identified with a global algorithm by Guan and Waliser (2015) in its revised version (Guan et al., 2018), adapted to the lower moisture content of the Arctic (Lauer et al., 2023).

2.4.2 Marine cold air outbreak index

A key feature of MCAOs are strong temperature decreases with increasing height especially in the lower troposphere over open ocean. This forms the basis for the MCAO index M to identify them and to quantify their strength. The MCAO index M was calculated following Papritz and Spengler (2017) and Dahlke et al. (2022):

$$M = \theta_{\text{SKT}} - \theta_{850} \tag{1}$$

with θ_{SKT} (θ_{850}) as the potential skin temperature (potential temperature at $850\,\text{hPa}$). Grid points with skin temperatures below $271.5\,\text{K}$ (i.e., over sea ice) were excluded from further processing as in Dahlke et al. (2022). We averaged over the central region and computed the climatology as for $\text{IVT}_{\text{north}}$. Following Papritz and Spengler (2017), MCAO conditions are present when $M > 0\,\text{K}$ and its strength can be classified as weak ($0\,\text{K} < M \leq 4\,\text{K}$), moderate ($4\,\text{K} < M \leq 8\,\text{K}$), strong ($8\,\text{K} < M \leq 12\,\text{K}$) or very strong ($M > 12\,\text{K}$).

2.4.3 Lower tropospheric parameters for marine cold air outbreak analysis

For a detailed analysis of the MCAO conditions over the campaign (Sect. 4.2), we used hourly ERA5 data of wind, temperature, and relative humidity at 850, 925, and $1000\,\text{hPa}$, as well as cloud cover, precipitation and surface turbulent heat fluxes (sensible and latent). All variables were temporally averaged over 6 hour intervals and spatially averaged over the central region. Cloud

cover was confined to open water surfaces only as ERA5 tends to overestimate especially low–level cloud cover over sea ice

155   (Di Biagio et al., 2021). Details can be found in Appendix A.

2.4.4   Environmental conditions of Polar Lows

We analyse the environment for Polar Low formation with a set of conditions (C1–C6) suggested by Radovan et al. (2019) and Terpstra et al. (2016) in a $200\,\mathrm{km}$ radius around the Polar Low's centre (pressure minimum): C1: sea surface temperature (SST) $- 500\,\mathrm{hPa}$ temperature, C2: SST $- 2\,\mathrm{m}$ temperature, C3: mean lapse rate below $850\,\mathrm{hPa}$, $C4_i$: mean relative humidity below

160     $950\,\mathrm{hPa}$, $C4_{ii}$: mean relative humidity between 850 and $950\,\mathrm{hPa}$, C5: $10\,\mathrm{m}$ wind speed (here, gust), C6: $500\,\mathrm{hPa}$ geopotential height anomaly. Condition C3 is evaluated as the vertical mean of the vertical potential temperature gradient between the surface and the $850\,\mathrm{hPa}$ pressure level. The meaning of each condition is summarized in Appendix A.

For conditions C1–C4, the 75th percentile, for C5, the maximum, and for C6, the mean were computed. Wahl et al. (2017) found that scales of multiples of the grid cell spacing are required to realistically represent the energy spectrum of a wind field.

165   We decided to use the maximum $10\,\mathrm{m}$ wind gust instead of mean wind to get a better estimate of the near–surface wind field of this small–scale phenomenon that might be hidden due to the coarse resolution of ERA5. The climatology of the $500\,\mathrm{hPa}$ geopotential height for C6 consists of all days of April between 1979 and 2022 for each grid point within the $200\,\mathrm{km}$ radius. Subsequently, the geopotential height anomaly was computed as the difference between the conditions during HALO–(AC)[3] and the climatology, and C6 was obtained by averaging over the $200\,\mathrm{km}$ circle.

170   Furthermore, we calculated vorticity from 10 dropsonde measurements taken within 1 hour arranged on a circular pattern. Following Lenschow et al. (2007) and Bony and Stevens (2019), we assumed horizontal variations in the wind field to be linear and expanded the wind vector with Taylor expansion around the centre of the circle in spherical coordinates.

2.4.5   Trajectory calculations

Trajectory calculations were performed using LAGRANTO (Sprenger and Wernli, 2015) and wind fields from ERA5. To assess

175   the origin of sampled cirrus air masses, 72 hour back–trajectories for the northernmost sections of the flights on 11 and 12 April were computed. Trajectories were initialized at the pressure levels 350–$550\,\mathrm{hPa}$ in $50\,\mathrm{hPa}$ steps, where the single–layer cirrus had been observed by HALO (Sect. 4.4). Furthermore, 72 hour back– and 48 hour forward–trajectories were computed to identify the pathways of the MWAIs (ARs) on 13 and 15 March (Appendix C). These trajectories were initialized along the $77.5°$ N latitude with $1°$ zonal spacing between $20°$ W and $13°$ E at 18:00 UTC on the respective days at the pressure levels

180   700, 850, and $925\,\mathrm{hPa}$.

3 Meteorological and sea ice conditions during HALO–(AC)[3]

3.1 Analysis and identification of synoptic events

In this section, we characterize weather events during HALO–(AC)[3] and assess their strength in the climatological context. At first, we separate the campaign into two major periods based on IVT_{north} and the MCAO index (M) in the central region (see Fig. 2). The campaign started with a warm and humid period with positive IVT_{north} and negative values of M, coinciding with enhanced static stability, from 11 to 20 March 2022. The warm period was followed by a cold and dry period from 21 March to 12 April 2022, where IVT_{north} (M) was almost exclusively negative (positive).

Within the warm and cold periods, we classified a large variety of weather events based on IVT_{north} and M, the large scale pressure constellation, and regional averages of meteorological variables from ERA5 (Fig. 3 and 4). In Fig. 5, we show latitude–averages of IVT_{north} and the vertically integrated meridional heat flux IHT_{north} over the central region to spatially and temporally localize meridional heat and moisture transport corresponding with MWAIs and MCAOs. Negative values of IHT_{north} and IVT_{north} indicate southward fluxes. To put the weather conditions into climatological context, anomalies of temperature at $850\,hPa$ and $2\,m$ above the surface, geopotential height at $500\,hPa$, and IWV were computed for the warm, cold and the entire campaign period. Positive (negative) anomalies correspond to values above (below) the long–term mean. Evaluating the temperature anomalies at these two levels reveals the vertical extent of the temperature anomalies in the lower troposphere.

3.1.1 Warm period

During the warm period, the corresponding general circulation pattern was characterized by a high surface pressure system extending from the North Sea to Baltic Sea and Scandinavia (Fig. 4a, b). The surface high was connected to a ridge in the $500\,hPa$ geopotential height. Low surface pressure and low $500\,hPa$ geopotential height were located over Greenland and the North Atlantic. This pressure constellation resulted in a consistent southerly and southwesterly flow with only a few short–lived interruptions in the three measurement regions. The interruptions can be seen as near–surface temperature drops and wind direction change (e.g., 11 March, Fig. 3c, d).

On 11–13 and 15–16 March, the pressure gradients between Greenland and Scandinavia were intensified and blocking (Omega Block) was established over most of Europe. Intense MWAIs are connected to blocking situations over the eastern border of a large basin (here, North Atlantic), redirecting cyclones northward as the typical eastward propagation is blocked (Woods et al., 2013). Consequently, warm and moist air masses originating from the North Atlantic were transported towards our three main measurement areas, driven by several low pressure systems that formed between Iceland and eastern Greenland.

We identified a strong MWAI event during the first week of the campaign (Fig. 3a) with area–averaged IVT_{north} up to $160\,kg\,m^{-1}\,s^{-1}$ (Fig. 2a). The event was detected as AR and passed through the measurement regions on 12–13 March (Fig. 4a). In the northern region, IWV reached its campaign maximum ($8\,kg\,m^{-2}$) on 13 March and declined afterwards while the $2\,m$ temperature in the northern region continued to increase until the following day (Fig. 3d, e).
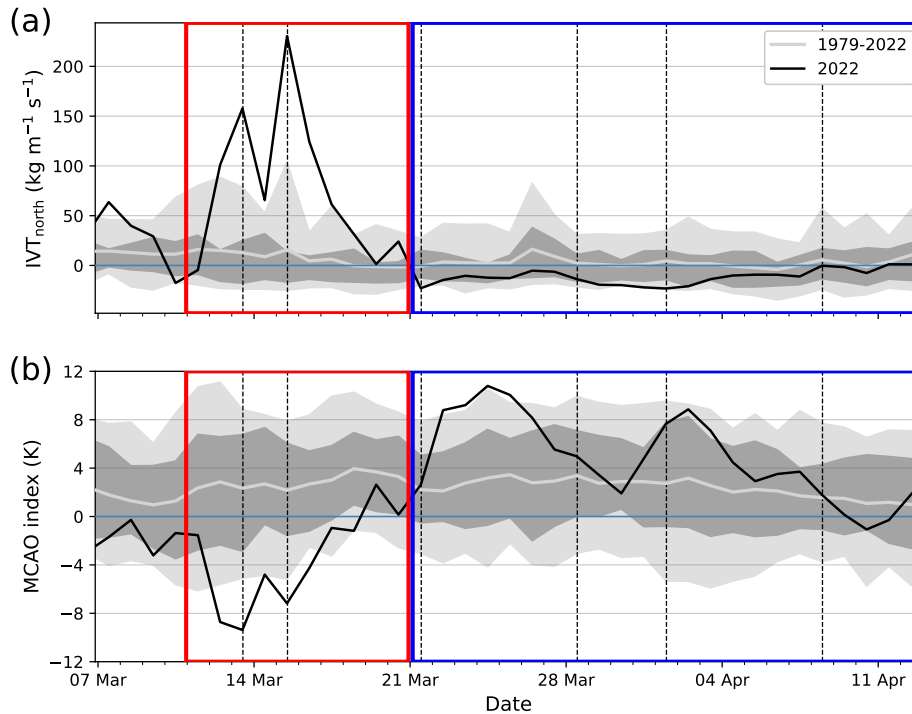
Figure 2. Daily means of (a) northwards component of integrated water vapour transport (IVT_{north}), (b) Marine Cold Air Outbreak (MCAO) index (M) based on ERA5 and averaged over the central region for HALO–(AC)^3 (black line). The mean, as well as the 10–90th and 25–75th percentiles of the climatology (1979–2022) are illustrated as grey line, light and dark grey shadings. The red (blue) box indicates the warm (cold) period dominated by MWAIs (MCAOs). Vertical dashed black lines mark the days shown in Fig. 4.

A second AR followed on 15 and 16 March (Fig. 3a), which had a more distinct confluent tropospheric southwesterly flow between the Greenland low and the Scandinavian high (Fig. 4b). In the central Arctic Ocean, the strongest warming occurred on 16 March and resulted in the highest 2 m temperature in March averaged over all ERA5 grid points north of 80° N (latitude–weighted) since 1979 (not shown). Simultaneously, the latitude–averaged IHT_{north} and IVT_{north} exceeded the previous maxima from 1996 ($9.44 \cdot 10^{10}$ W m^{-1} vs. $9.32 \cdot 10^{10}$ W m^{-1}, and 388 kg m^{-1} s^{-1} vs. 384 kg m^{-1} s^{-1}, Fig. 5). In some parts of the northern region, near–surface temperatures were above freezing and even liquid precipitation was documented over the sea ice (Fig. 3c, f, analysed in greater detail in Sect. 4.1). The AR on 15–16 March also caused the highest daily precipitation of the northern region over the campaign period. In the central region, the area–averaged 2 m temperature was above freezing and a high fraction of rainfall to the total daily precipitation was found.

After the AR, much drier but still relatively warm air followed, leading to a strong reduction in IVT_{north} and a slight reduction in IHT_{north} (Fig. 5). As a surface based high pressure system formed over Greenland, the large–scale pressure constellation started to change. However, at upper levels, low geopotential persisted, promoting the formation of a strong low pressure
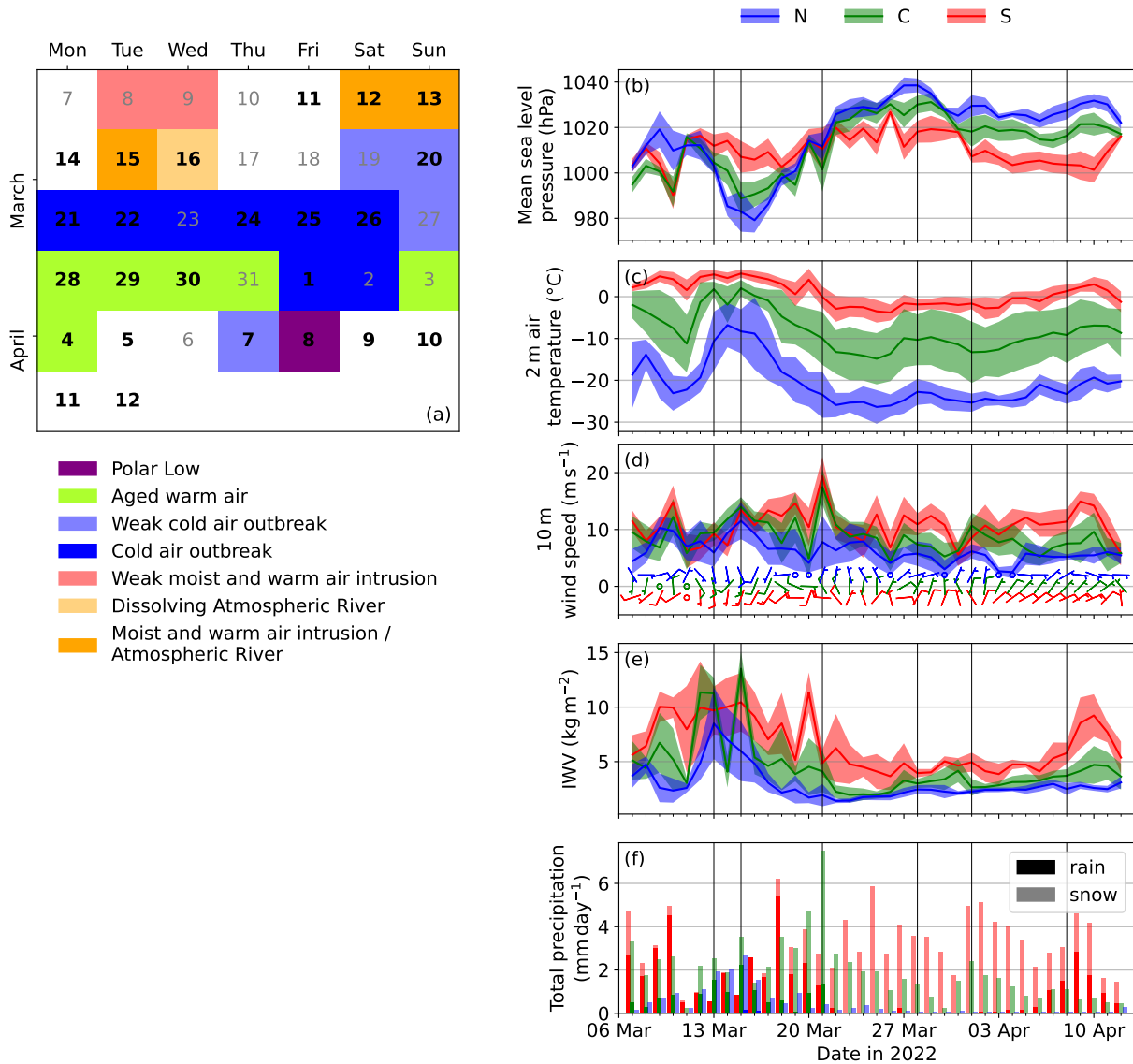
Figure 3. Left column: (a) Calendar of March and April 2022 showing the categorized and colour-coded weather conditions. Bold font indicates days when research flights were performed. Right column: Regional averages (lines) and standard deviation (shading) of ERA5 based time series of (b) mean sea level pressure, (c) 2 m temperature, (d) 10 m wind (lines indicate speed, barbs indicate direction and speed), (e) integrated water vapour (IWV), and (f) daily accumulated precipitation, separated into rain (no transparency) and snow (partly transparent). Regional averages are performed for the southern (S, red), central (C, green), and northern (N, blue) region shown in Fig. 1. Vertical black lines indicate days shown in Fig. 4.

system near Iceland on 20 March. The low quickly propagated towards the northeast and was characterized by rapid deepening ($> 25\,\mathrm{hPa}$ core pressure decrease in 24 hours) and a frontal structure representative of a Shapiro–Keyser cyclone (Shapiro and Keyser, 1990). On the eastern flank of the Shapiro–Keyser cyclone, $\mathrm{IHT_{north}}$ and $\mathrm{IVT_{north}}$ indicate similarly strong fluxes as on 12 March (Fig. 5).

In the climatological perspective, the prevailing pressure gradient between Scandinavia and Greenland is reflected in the extremely strong gradient of the $500\,\mathrm{hPa}$ geopotential height anomalies ($> 10\,\mathrm{gpdm}$ over Scandinavia, $< -10\,\mathrm{gpdm}$ over Greenland, Fig. 6h) and was responsible for the associated warming. Moreover, we found positive temperature anomalies at $850\,\mathrm{hPa}$ of more than $7\,\mathrm{K}$ over the Fram Strait and up to $9\,\mathrm{K}$ over Scandinavia and around Franz Josef Land (northeast of Svalbard, Fig. 6b). At $2\,\mathrm{m}$, the warming was amplified to more than $16\,\mathrm{K}$ above climatology over Franz Josef Land and more than $10\,\mathrm{K}$ over the Greenland Sea and Fram Strait (Fig. 6e). The bottom–amplified warming is consistent to the findings of Woods and Caballero (2016), confirming the reduction of the Arctic boundary layer inversion strength through intense MWAIs. Additionally, the high amounts of moisture carried by the ARs resulted in positive IWV anomalies of more than $2\,\mathrm{kg\,m^{-2}}$ over the southern, central, and parts of the northern region (up to $4\,\mathrm{kg\,m^{-2}}$ in the Norwegian and Greenland Seas, Fig. 6k).

3.1.2 Cold period

On 21 March 2022, the Shapiro–Keyser cyclone, together with a strong high pressure system over Greenland, marked a turning point in the circulation pattern (Fig. 4c). Compared to the warm period, the zonal pressure gradient across the North Atlantic has been inverted. The resulting northerly winds caused negative $\mathrm{IHT_{north}}$ and $\mathrm{IVT_{north}}$ after the cyclone passed (Fig. 3d and 5). Although the sign of the pressure gradient remained until the end of the campaign (12 April), the position and strength of the synoptic– and meso–scale circulations changed over time. As Kolstad et al. (2009) showed, there is a connection between such a circulation pattern and the onset of MCAOs in that region. In all three measurement regions, the area–averaged $2\,\mathrm{m}$ temperature remained below $0\,^{\circ}\mathrm{C}$ until 07 April (Fig. 3c).

As the Shapiro–Keyser cyclone stayed over the Barents Sea while dissipating, IWV dropped to the lowest area–averaged values in the northern region (1.4–$2.4\,\mathrm{kg\,m^{-2}}$, Fig. 3e). Two strong MCAO events were observed during the cold period. The first one lasted for almost the entire third campaign week with a maximum M of $10\,\mathrm{K}$, which exceeded the 90th percentile of the climatology (Fig. 2b).The second MCAO event occurred on 01–02 April and exceeded the 75th percentile with M up to $9\,\mathrm{K}$. This event showed the minimum latitude–averaged $\mathrm{IHT_{north}}$ of the campaign ($-5.32 \cdot 10^{10}\,\mathrm{W\,m^{-1}}$, Fig. 5) and did not reach the 0.02^{th} percentile of the climatology.

Between the two strong MCAO events and after the second one, the MCAO conditions weakened (decreasing M) in the western Fram Strait due to decreasing pressure gradients and calming winds, which turned more towards easterlies (Fig. 3d). Especially in the central region, the near–surface temperature increase (Fig. 3c) indicated the advection of relatively warm air from several subpolar regions across the central Arctic. We classified these events as aged warm air periods (Fig. 3a) during which we observed mainly three recurring patterns. First, the easterly winds resulted in cloud–free areas in the lee of Svalbard. Second, converging winds over the central Fram Strait led to increased convective cloud formation. Third, some cloud streets developed over the western Fram Strait due to a less disturbed off–ice flow. Both position and intensity of these patterns varied
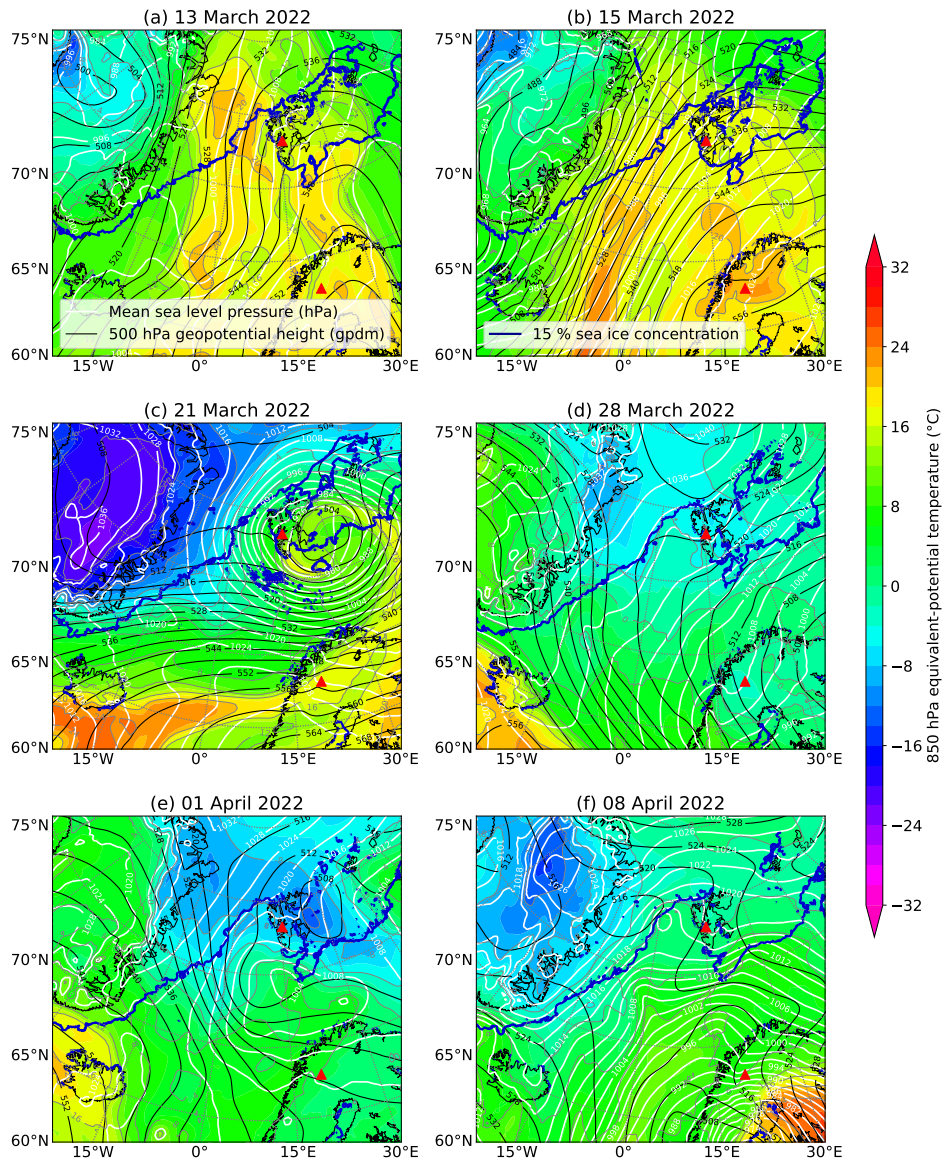
Figure 4. Maps of mean sea level pressure (white contour lines), $500\,\text{hPa}$ geopotential height (black contour lines), and $850\,\text{hPa}$ equivalent–potential temperature (shading and grey contours) from ERA5 data for representative days of the main weather conditions at 12 UTC. 13 March (a) and 15 March (b) represent the moist and warm air intrusions with AR characteristics, (c) shows the Shapiro–Keyser cyclone on 21 March that marked the beginning of the cold air outbreak period, 28 March (d) and 01 April (e) represent the persistent northeasterlies with varying cold air advection strength, and (f) features the Polar Low west of Svalbard on 08 April. The $15\,\%$ sea ice concentration from AMSR2 (Spreen et al., 2008) is displayed as blue contour line.
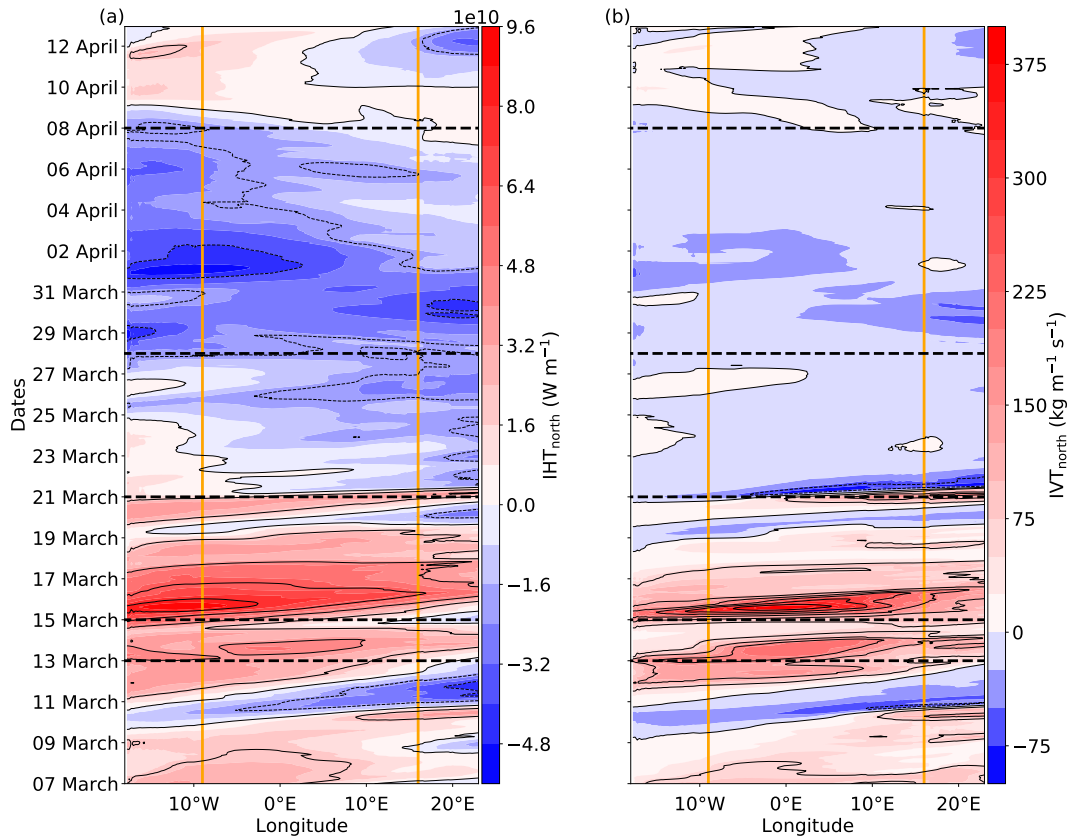
Figure 5. Hovmöller diagram of hourly vertically integrated meridional fluxes of (a) heat (IHT_{north}), and (b) moisture (IVT_{north}) during HALO–(AC)[3], averaged over the central region latitudes. Positive (negative) values indicate northward (southward) fluxes. Orange vertical lines indicate the longitude boundaries of the central region. Important synoptic events shown in Fig. 4 are marked by horizontal dashed lines. Data is based on ERA5.

from day to day. On 05–06 April, the relatively warm air was still present in the measurement regions, but the advection was
260   weaker due to reduced horizontal pressure gradients. Therefore, we did not attribute these days to one of the weather classes
defined in Fig. 3.

On 07 April, another weak MCAO (Fig. 2b) and the positive vorticity of an upper–level trough reaching Fram Strait promoted
the formation of a mesoscale cyclone with features of a Polar Low (Fig. 4f, details in Sect. 4.3). In the following two days, the
Polar Low moved to the northwest and dissipated over the sea ice northeast of Greenland. In parallel, a low pressure complex
265   over Scandinavia advected warm and moist air from Siberia towards the Norwegian Sea. This air mass caused an increase of
IWV above $10\,\mathrm{kg\,m^{-2}}$ over parts of the southern region (Fig. 3e) and was advected northwards with a southerly upper–level
flow in the following days (10–12 April). The elevated moist air led to the formation of cirrus clouds over the western Fram
Strait (see Sect. 4.4).

Overall, the period of pronounced MCAO activity lasting from 21 March to 12 April much better reflects the typical state of the central region than the preceeding warm period. Climatologically, the entire campaign period is characterized by weak MCAO conditions (M between 1 and 3 K). With a duration of 5–6 days, the first HALO–(AC)^3 MCAO period (21–26 March) was slightly longer than the mean duration of MCAO events (3–4 days, Terpstra et al., 2021). During the cold period, the 500 hPa geopotential height anomalies were negative over Scandinavia and northwestern Russia (coinciding with low surface pressure), and positive over the central Arctic and Greenland (coinciding with high surface pressure, Fig. 6i). The persistence of the northerly winds due to this anomalous pressure constellation explains the longevity of the MCAO conditions. Negative temperature anomalies at 2 m and at 850 hPa were most prominent in the central Fram Strait, Norwegian Sea and parts of the Greenland Sea, which were affected by the cold air advection (Fig. 6c, f). Reduced IWV compared to the climatology overlaps well with the negative 850 hPa temperature anomalies (Fig. 6l). Positive temperature anomalies at 850 hPa were restricted to regions that were not affected by cold air advection (central Arctic, eastern Barents Sea). Interestingly, the central Arctic Ocean showed negative temperature anomalies at 2 m and positive anomalies at 850 hPa, suggesting enhanced static stability compared to the climatological mean (Fig. 6c, f). This area also shows slightly positive subsidence anomalies at 850 hPa (not shown). In contrast, the static stability is reduced in the area between Svalbard and Franz Josef Land with positive anomalies at the surface and negative anomalies at 850 hPa.

3.1.3 Climatological assessment of the full HALO–(AC)^3 period

The 2 m temperature anomalies for the entire HALO–(AC)^3 period (07 March–12 April) were positive in most regions shown in Fig. 6d. Only in the central Fram Strait and north of Greenland negative 2 m temperature anomalies down to -1.2 K and -2.4 K, respectively, were found, coinciding with the regions of strongest negative 2 m temperature anomalies during the cold period. Slightly positive 2 m temperature anomalies over the sea ice in the western Fram Strait indicate that the extremely positive anomalies of > 8 K during the warm period were not completely balanced by negative anomalies during the longer cold period (Fig. 6d–f). Temperature anomalies at 850 hPa were positive in all regions shown in Fig. 6. The strongest anomalies with 2–3.5 K were found over the central Arctic Ocean and northern Barents Sea, coinciding with the regions of positive 850 hPa temperature anomalies during the cold period (Fig. 6a, c). Positive temperature anomalies combined with high surface pressure over Scandinavia (central Arctic) in the warm (cold) period resulted in overall positive 500 hPa geopotential height anomalies over these regions (Fig. 6g). The lowest 500 hPa geopotential height anomalies were located over the east coast of Greenland, where low geopotential also remained during the first part of the cold period.

Over the central region, we found small northward heat fluxes (IHT$_{\text{north}}$ of $5.4 \cdot 10^8$ W m^{-1}) and moisture fluxes (IVT$_{\text{north}}$ of 18 kg m^{-1} s^{-1}). Consequently, the thermal energy input into the Arctic through this pathway was slightly positive and the brief but intense MWAIs / ARs overcompensated the long MCAO period. In previous years, IHT$_{\text{north}}$ and IVT$_{\text{north}}$ were often smaller or even negative over the campaign days and the central region.
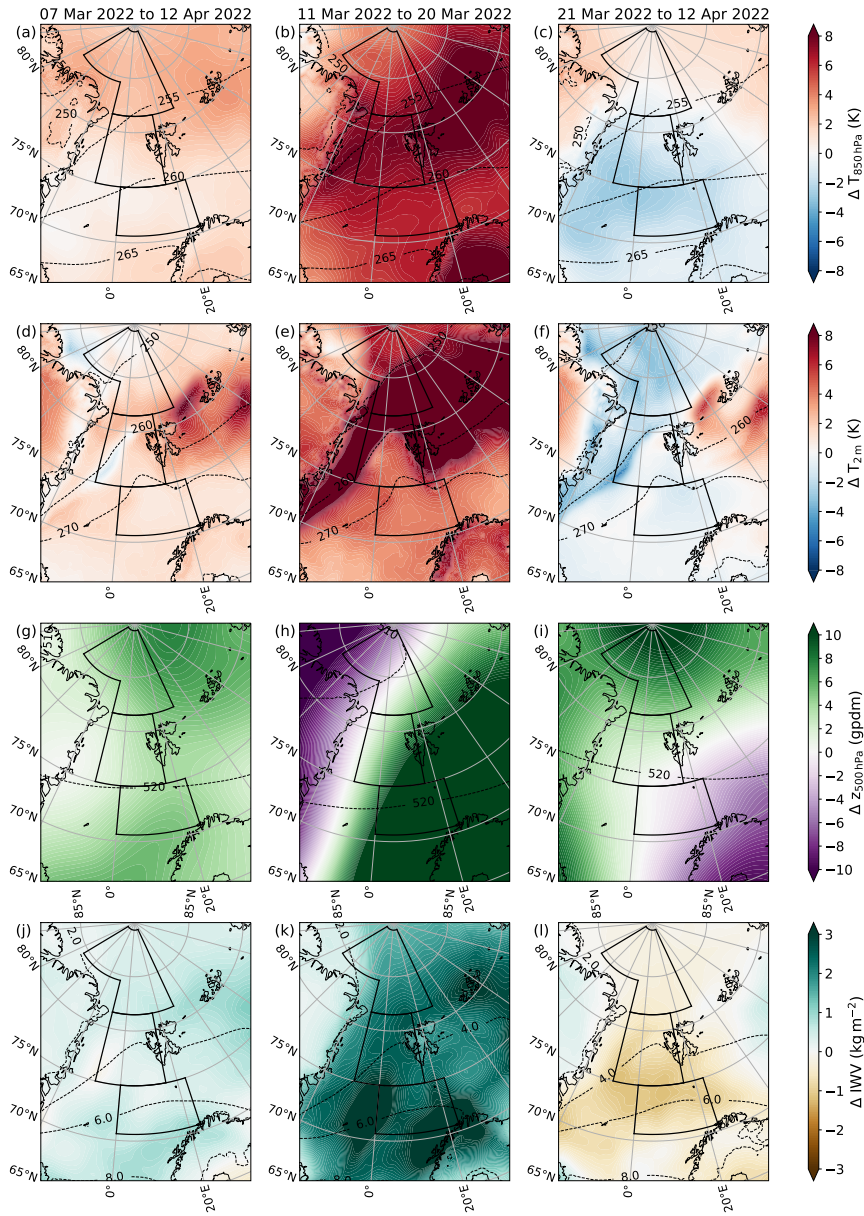
Figure 6. Anomaly maps of (a–c) temperature at $850\,\text{hPa}$ ($\Delta T_{850\,\text{hPa}}$), (d–f) $2\,\text{m}$ temperature ($\Delta T_{2\,\text{m}}$), (g–i) geopotential height at $500\,\text{hPa}$ ($\Delta z_{500\,\text{hPa}}$), and (j–l) vertically integrated water vapour (ΔIWV) based on ERA5 for the entire campaign, the warm, and the cold period in the left, middle, and right column. The coloured contours show the long--term mean subtracted from the mean of the time period in 2022 so that positive (negative) values correspond to anomalies above (below) the long-term mean. The dashed black isolines describe the long—term climatology in each panel. The three measurement regions (shown in Fig. 1) are illustrated as black boxes.

3.2 Ny–Ålesund

The extensive remote sensing observations at Ny-Ålesund may complement the airborne observations during HALO–(AC)[3]. However, Ny-Ålesund is located at the eastern edge of the central region and measurements may be influenced by the local orography. Based on the temperature profiles (Fig. 7a), the atmospheric conditions at Ny–Ålesund can also be divided into a warm (11–21 March) and a colder period (22 March–12 April). Compared to the full central region, this indicates a temporal shift of one day.

The warm air advection related to the first AR led to an increase of $2\,\mathrm{m}$ temperature from about $-14\,^{\circ}\mathrm{C}$ to $+2\,^{\circ}\mathrm{C}$ within 19 hours (meteorological tower measurements, not shown). Vertical advection of heat and moisture lifted the tropopause to $12.9\,\mathrm{km}$ (measured by the 12 UTC radiosonde on 12 March, Fig. 7a). The $2\,\mathrm{m}$ temperature remained above freezing for five days and even reached a new maximum for March on 15 March ($5.5\,^{\circ}\mathrm{C}$). On this day, also the highest IWV was observed ($14.5\,\mathrm{kg\,m^{-2}}$, Fig. 7b).

The warm period was characterized by constant low–level cloud cover over Ny–Ålesund detected by the ceilometer, interrupted only by a few hours of high–level cloud occurrence in connection with a high pressure ridge passing the site in the night of 14–15 March (not shown). The situation changed during the course of 17 March, when the cloud deck started to dissolve and the $2\,\mathrm{m}$ temperature dropped below $0\,^{\circ}\mathrm{C}$.

The influence of the Shapiro–Keyser cyclone (see Sect. 3.1) delayed the beginning of the cold period over Svalbard compared to the central region by about one day. Northerly winds corresponding to the MCAO period led to extremely dry conditions with IWV down to $1.1\,\mathrm{kg\,m^{-2}}$ (closest grid point in ERA5 with land–fraction < 0.25: $1.5\,\mathrm{kg\,m^{-2}}$) on 24 March at 06 UTC (Fig. 7b). This IWV is below the 3rd percentile of all radiosondes between 07 March and 12 April 1993–2022 (Maturilli and Kayser, 2016, 2017; Maturilli, 2020b). At Ny–Ålesund, the MCAO conditions on 23–30 March, and on 01–05 April were mostly associated with clear sky and $2\,\mathrm{m}$ temperatures below $-12\,^{\circ}\mathrm{C}$. Aged warm air reached Ny–Ålesund on 28–29 March with more humidity, with slightly higher temperatures and IWV increasing to $4\,\mathrm{kg\,m^{-2}}$.

Especially during the cold period, cloud conditions at Ny–Ålesund are not representative for the central region because of lee effects as visible on MODIS images (e.g., NASA Worldview, not shown). Additionally, the temporal delay related to the propagation of synoptic systems during the warm period must be kept in mind when combining Ny–Ålesund with HALO–(AC)[3] observations.

3.3 Sea ice conditions

The different synoptic patterns affected the sea ice conditions in the measurement areas. In Fig. 8a–c, we present the spatial distribution of SIC before (09–11 March) and during (14–16 March) the MWAIs, as well as after the MCAO period (10–12 April). SIC was $> 90\,\%$ in almost the entire northern region in the first period (Fig. 8a). In the central region, the sea ice covered 30–40 % of the area with a southwest–northeast oriented edge. The southern region was almost completely ice–free over the entire campaign duration (Fig. 8a–c). A time series of SIC for the central region compared to the climatology is shown in Fig. 8d.
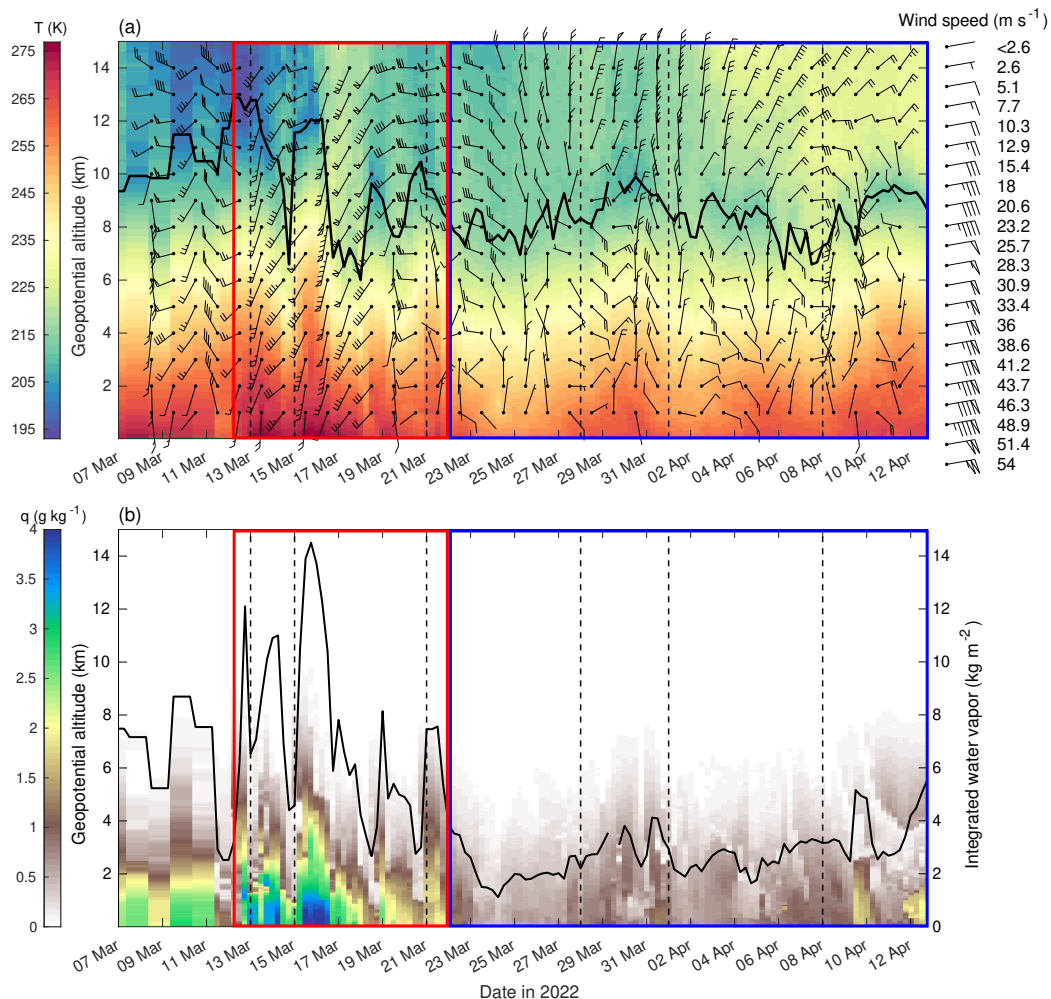
Figure 7. Time series of Ny–Ålesund radiosondes of (a) temperature profiles (shading), height of thermal tropopause (black line), and wind barbs in selected levels, and (b) specific humidity profiles (shading) and resulting IWV (black line, right axis). Vertical dashed black lines indicate the days shown in Fig. 4. The red (blue) box indicates the shifted warm (cold) period.

The MWAI / AR events on 12–13 and 15 March caused a reduction of SIC in the northwestern part of the central region, resulting in the lowest values of the entire campaign period (Fig. 8b, d). SIC was below the climatological mean but within the 10–90th percentiles. Furthermore, an unusually large polynya opened from north of Svalbard to Franz Josef Land, which resulted in the below–average static stability during the cold period in this region (Fig. 8b). We assume that ice dynamics related to strong winds caused the SIC decrease, but ice melt cannot be excluded as well because temperatures were above freezing and liquid precipitation was observed over sea ice. Rapid ice melt has been attributed to warm air advections and induced increases of heat flux in summer (Tjernström et al., 2015; Woods and Caballero, 2016). Although the liquid precipitation on snow alters

335

340 the signal of the microwave radiometry and might have increased the uncertainty of the SIC product (Stroeve et al., 2022; Rückert et al., 2023), that SIC reduction was obvious in visual satellite images as well (e.g., NASA Worldview, not shown). After the AR events, the sea ice conditions recovered and the polynya closed again (Fig. 8c, d) mostly due to sea ice transport from the central Arctic. This southward transport can be attributed to the winds during the high MCAO activity between 21 March and 07 April.

345   For most of the campaign period, the average SIC in the central region was above the climatological mean (Fig. 8d). A map of SIC anomalies compared to the climatological mean is illustrated in Fig. 8e. Southwest of $75°$ N and $0°$ E as well as northeast and southeast of Svalbard, SIC anomalies were negative. In contrast, a positive SIC anomaly was found in the central and western Fram Strait, which overlaps well with the negative $2\,\mathrm{m}$ temperature anomalies shown in Fig. 6d, f. The west coast of Svalbard used to be covered by ice in the climatology but was completely ice–free during HALO–(AC)[3]. In the northern

350 and southern regions, the mean SIC for the entire campaign period did not differ more than $5\,\%$ from the climatological mean.

    Note that uncertainties in the marginal ice zone are especially large due to weather related filters and as a result of temporal and spatial interpolations. This mainly affects the central region where the estimated uncertainties of the SIC product (total standard uncertainty) can reach up to $40\,\%$ at the ice edge, mostly due to smearing uncertainty (gridding of the swaths, i.e., areas imaged on the surface, from several daily overflights), and different satellite footprints at different frequency channels.
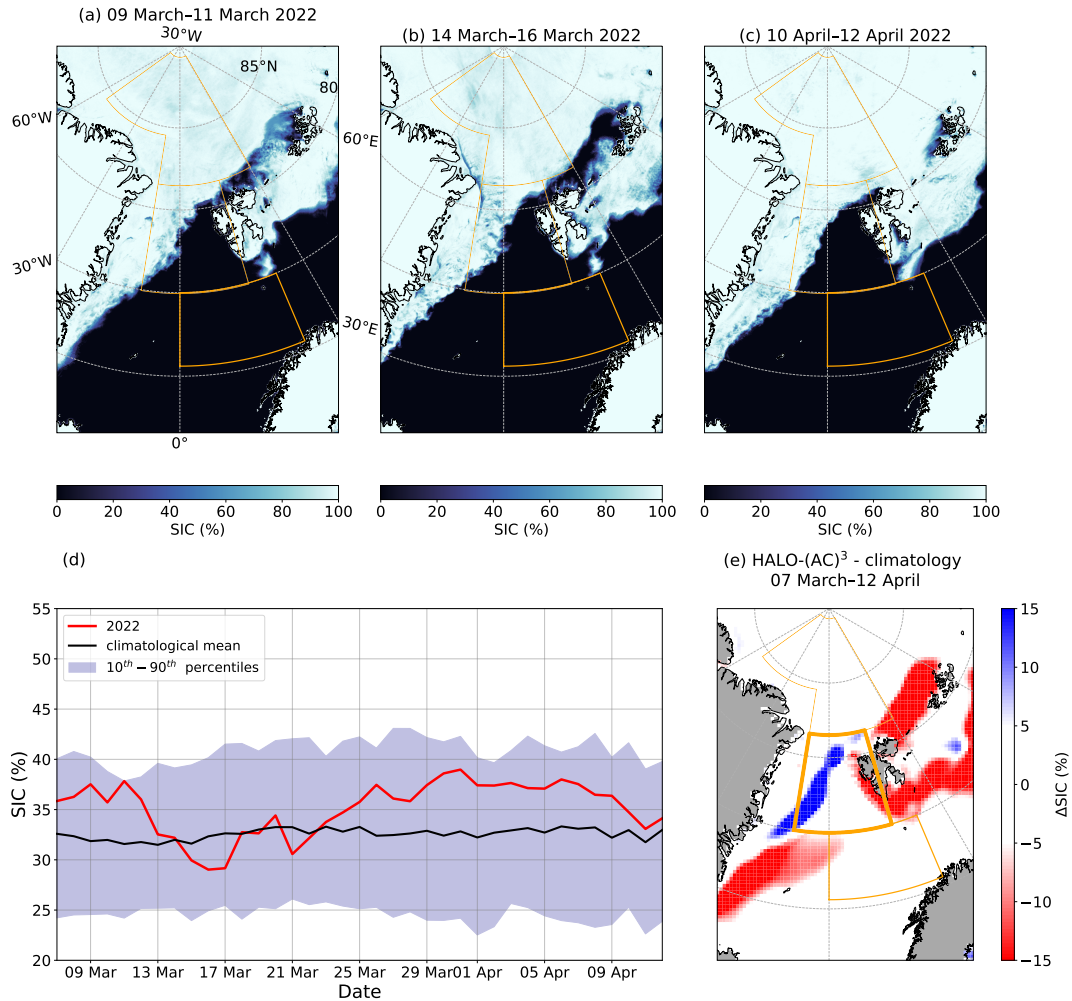
Figure 8. Average sea ice concentration (SIC) from the MODIS-AMSR2 product at 1 km grid resolution for (a) 09–11 March (prior to the first AR event), (b) 14–16 March (during the second AR event), (c) 10–12 April (at the end of the campaign). Data is from the MODIS-AMSR2 product at 1 km grid resolution. (d): SIC time series averaged over the central region for the campaign period, as well as the mean, and 10–90th percentiles of the 1979–2022 climatology. (e): SIC anomalies from the climatological mean averaged over the entire campaign period. Note that only differences larger 5 % are considered due to the uncertainties of the satellite product in the marginal ice zone. Data for (d) and (e) is from the OSI–SAF sea ice concentration climate data record.

4 Specific events during HALO–(AC)^3

4.1 Warm air intrusions and Atmospheric Rivers

The warm period was characterized by four independent AR events (12–13 March, 14 March, 15 March, and 20 March) that were at least partly sampled by research aircraft in the three measurement regions. Back trajectory analyses with LAGRANTO (Sect. 2.4.5) revealed that the air masses of the 12–13 March event (Fig. B1a) originated from mid–latitude regions of the North Atlantic and from central Europe (Fig. C1a). For the second AR event on 15 March (Fig. B1b), the air masses originated almost exclusively from the western part of the mid–latitude North Atlantic (Fig. C1b). We neglect the ARs on 14 and 20 March as they did not enter the central region, but either propagated northwards to the west of it or dissipated before reaching it. The moist air advection event on 10 April (Fig. C1c) was too weak to be identified as AR, but was relevant for the formation of cirrus clouds over sea ice.

We compare the strength of AR events during HALO–(AC)^3 by analysing them with respect to the relation between IVT and latitude over the North Atlantic and Arctic Ocean (50–90° N, 60° W–40° E) (Fig. 9). Note that a different region was selected to extend the view on the North Atlantic, one of the major pathways of ARs (Guan and Waliser, 2017; Nash et al., 2018). Along their northward propagation, ARs generally decline in intensity. If otherwise ARs start to form in the Arctic, their moisture supply is reduced so that their intensification is limited (Papritz et al., 2021). Therefore the number of strong AR events decreases meridionally (Fig. 9).

North of 70.6° N (southern boundary of the southern region), only few ARs exceed an IVT of $250\,\mathrm{kg\,m^{-1}\,s^{-1}}$ when averaged over the detected AR area (Fig. 9). In the climatology, the majority has mean values around $150\,\mathrm{kg\,m^{-1}\,s^{-1}}$. The AR events on 12–13, and 15 March represent strong cases in terms of mean IVT for all time steps as they lie outside the 25$^{\text{th}}$ percentile in latitude–IVT space (Fig. 9). On 15 March at 18 UTC, the AR averaged IVT even exceeded the 10$^{\text{th}}$ percentile while being centered at 76° N. While the AR centre from the event on 12–13 March was located most northerly before it dissipated, the AR from 15 March was characterized by the most intense moisture transport with mean IVT of around $250\,\mathrm{kg\,m^{-1}\,s^{-1}}$ when centered at 70° N, decreasing to $200\,\mathrm{kg\,m^{-1}\,s^{-1}}$ at 75° N. Maximum IVT (meridional and zonal) slightly exceeded $400\,\mathrm{kg\,m^{-1}\,s^{-1}}$ between 13 and 16 March in the central region (see Appendix B, Fig. B1). HALO's dropsonde measurements showed a maximum IVT of $490\,\mathrm{kg\,m^{-1}\,s^{-1}}$ on 15 March, suggesting that ERA5 underestimates the moisture flux. As these AR events had meridionally elongated structures, the outflow region reached up to the central Arctic while their centres were located at 70–78° N (Fig. 9). During their poleward propagation, the moisture transport decreased so that they no longer fulfilled the detection requirements.

The AR events in the warm period were associated with anomalous amounts of precipitation. In Fig. 10, we show the hourly averaged precipitation rate from 11 to 20 March 2022 as well as for the climatology of these days. Along the east coast of Greenland, the total precipitation and snowfall rate partly exceeded $1\,\mathrm{mm\,h^{-1}}$ (Fig. 10a, d), around six times higher compared to climatology (Fig. 10c, f). Over the North Atlantic, Fram Strait, and central Arctic Ocean, total precipitation and snowfall rates exceeded the climatology by a factor of 3. Record breaking rainfall rates were found northwest of Svalbard, exceeding the climatology up to a factor of 36 (Fig. 10i). However, the actual rainfall rate in this area was below $0.25\,\mathrm{mm\,h^{-1}}$ and the

high deviation is caused by even lower rainfall rates in the climatology. Liquid precipitation over sea ice was also observed by
390   the cloud radar onboard HALO during research flights.

In summary, the ARs observed during HALO–(AC)[3] featured uncommonly high AR–averaged IVT values, higher than 90% of all ARs in the climatology. Additionally, record breaking rainfall rates occurred over the sea ice northwest of Svalbard.
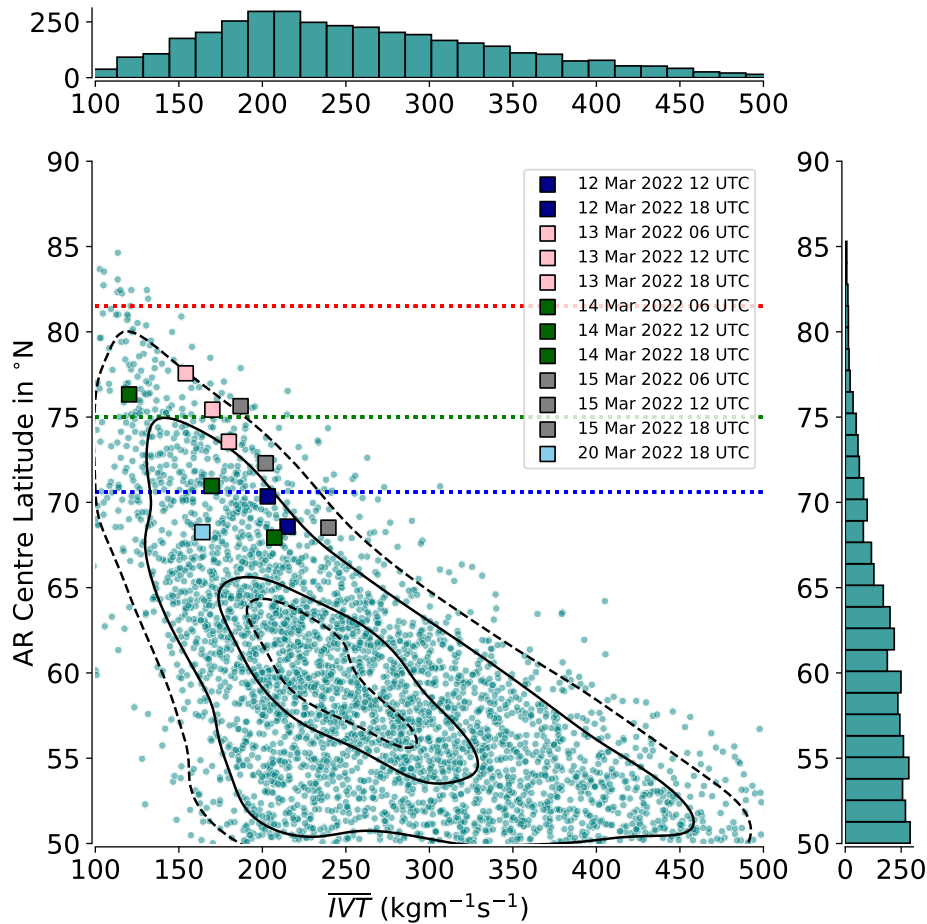
Figure 9. Six hourly climatological (1979–2022) distribution of central latitudes of Atmospheric Rivers (ARs) as a function of mean AR IVT using an ERA5 based AR catalogue modified from Guan and Waliser (2015). Cases categorized as ARs during HALO–(AC)[3] are illustrated by coloured boxes for 06, 12, and 18 UTC of respective flight days. Black (dashed) lines indicate the 25th and 75th (10th and 90th) percentiles of a kernel density estimation to visualize the shape of the histogram. Horizontal dotted lines indicate the latitude boundaries of the three measurement regions (Fig. 1) in the same colours as in Fig. 3.
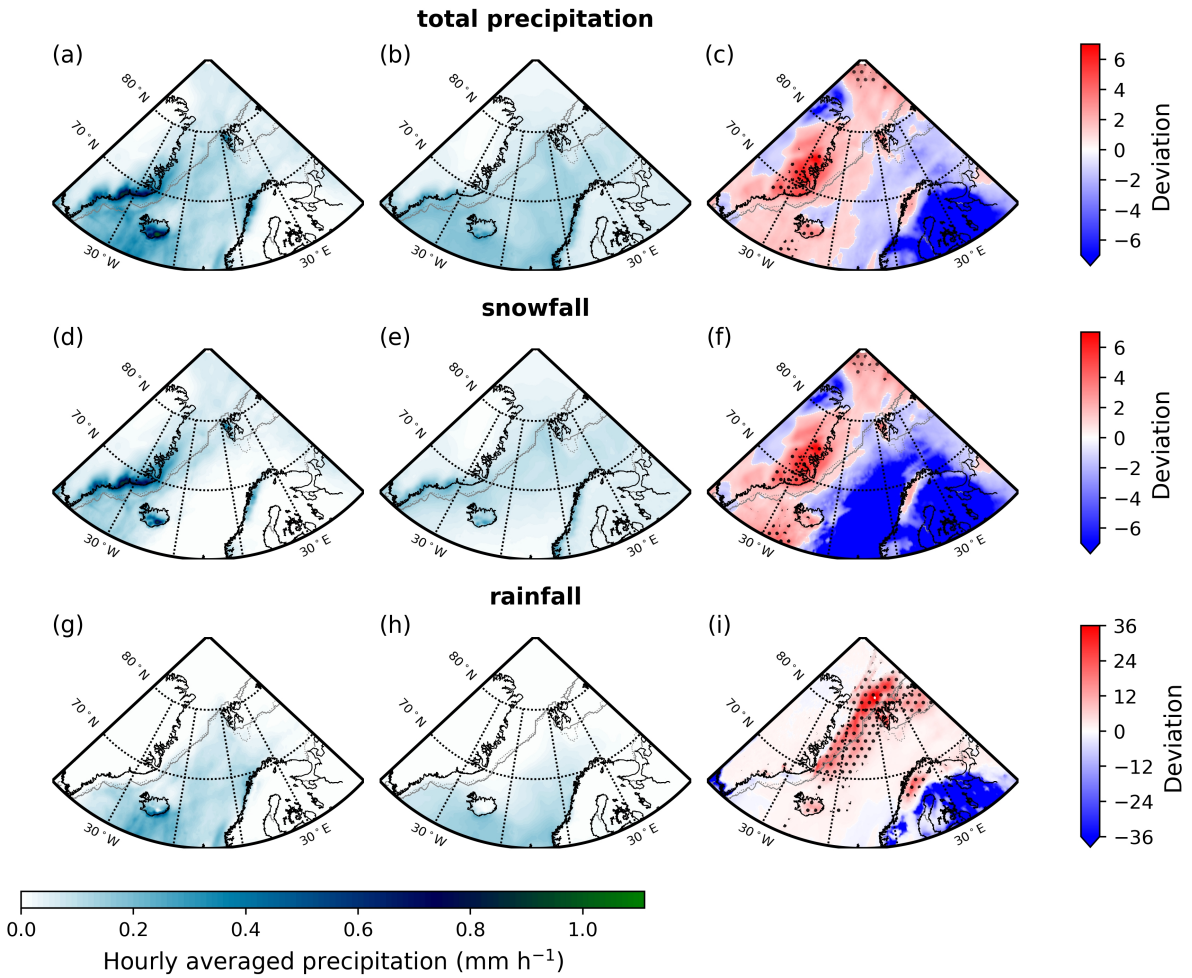
Figure 10. Hourly averaged precipitation, snowfall and rain rate $(\mathrm{mm\,h^{-1}})$ derived from ERA5 for (a, d, g) 11–20 March 2022, and (b, e, h) the climatology. In (c, f, i), we show the deviation from the climatology. Note that the rainfall over sea ice is barely visible in both (g) and (h). Positive deviations of precipitation rates are illustrated as the fraction of the average rate in 2022 to the rate of the climatology while negative deviations are given as its inverse.

4.2 Marine cold air outbreaks

The cold period included several MCAO events (21 March–07 April), which are analysed in detail specifically for the central region. Figure 11 shows the time series of atmospheric conditions as described in Sect. 2.4.3. To highlight the conditions in the MCAOs' source region, we also include the temporal evolution of the parameters averaged over the eastern part of the northern region in Appendix D (Fig. D1). The corresponding temporal development over the southern region is shown in Fig. D2 in Appendix D.

After the Shapiro–Keyser cyclone, which caused multi–layered clouds and intense snowfall on 21 March at the west coast of Svalbard (Fig. 11d–g), MCAO conditions were established. From 22 to 26 March, the contribution of convective to total snowfall increased over open water and mid– and high–level cloud cover decreased. Over sea ice, the total snowfall was low and almost exclusively stratiform. Liquid precipitation was not present except for 21 March. Low–level cloud cover remained high until 07 April, reflecting the presence of the atmospheric boundary layer clouds typically associated with MCAOs (Fig. 11d).

The strong MCAO events (21–26 March and 01–02 April) were characterized by the strongest northerly lower tropospheric winds and high values of domain–averaged turbulent fluxes of sensible and latent heat flux (Fig. 11a, h). The maximum values of sensible and latent heat coincided with the highest wind speeds and low temperatures (21–22 March, Fig. 11a, b, h). Note that over the southern region the sensible heat fluxes were slightly lower, whereas, on average, latent heat fluxes were higher than over the central region (Fig. D2). Near–surface air temperatures increased towards the south, resulting in smaller sensible heat fluxes while latent heat fluxes were increased due to a rising saturation water vapour pressure at the air–sea interface (e.g., Hartmann et al., 1997). We found that larger differences between the specific humidity of the air and specific humidity at saturation in the southern compared to the central region were responsible for the increased latent heat fluxes (not shown).

During the weak MCAOs and aged warm air periods, northeasterly winds dominated (Fig. 11a). Compared to strong MCAO conditions, sensible heat fluxes were reduced by a factor of 2 while latent heat fluxes decreased to a lesser extent. Between 27–30 March and 03–05 April, when aged warm air was advected to the central region, precipitation decreased as the air mass dried and temperatures increased (Fig. 11b, c, g). Also, foehn effects due to the easterly winds over Svalbard might have contributed to drier and warmer conditions over parts of the Fram Strait as this effect can influence the atmospheric conditions more than 100 km off the coast (Shestakova et al., 2022). The eastern parts of the central region close to Svalbard were not fully covered by low–level clouds as the 5 % percentile was mostly between 0.2–0.4. For the first aged warm air period, the southward advection of the air masses from the sea ice covered ocean took about one day. This can be seen when comparing the temporal evolution of the lower tropospheric temperature and relative humidity over the northern and central regions (i.e., low relative humidity from 29 to 30 March, Fig. D1a–c vs. 11a–c).

From 05 April on, the mean wind speed decreased and turned to northeast. Hence, more convergent regions developed in the lee of Svalbard with a rather diffuse low–level cloud structure (not shown). These converging winds in combination with a weak MCAO promoted the formation of a Polar Low in the following days, which is explained in greater detail in the next section. Hence, different wind regimes ranging from northwest to northeast and MCAO strengths were observed during HALO–(AC)[3]. The large variety of MCAO conditions provides great opportunities for detailed cloud evolution and air mass transformation studies.

4.3 Polar low

The Polar Low formed on 07 April close to the west coast of Svalbard at a baroclinic zone where cold air transported by northeasterly winds converged with warmer North Atlantic air from south to southeasterly winds. During the development phase of the Polar Low, the mean sea level pressure showed closed isobars from 08 April 00 UTC on (Fig. 4f). We examine
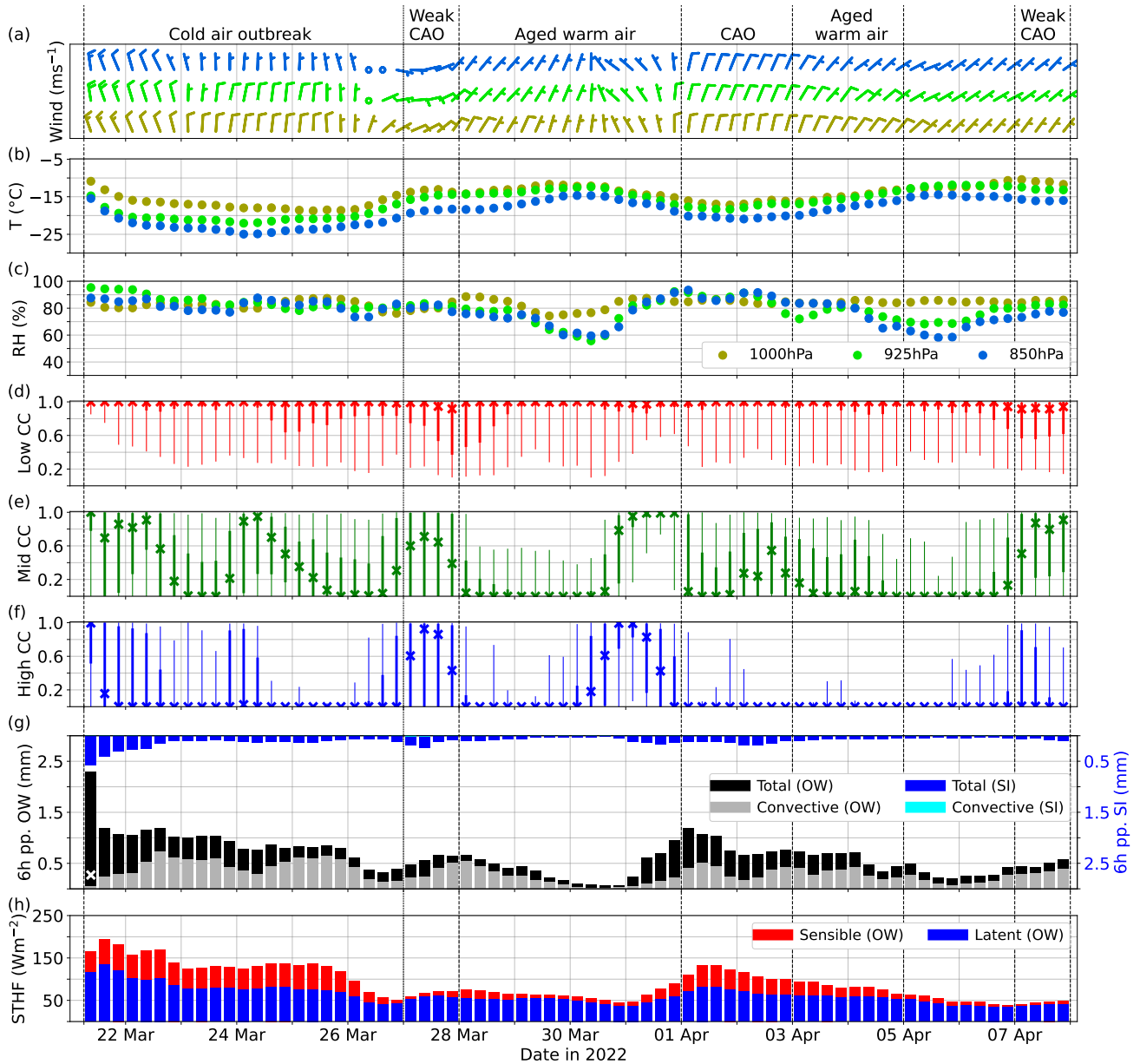
Figure 11. Temporal evolution of (a) wind, (b) air temperature (T), and (c) relative humidity (RH) on the 1000, 925, and 850 hPa pressure levels, and of (d) low–, (e) mid–, and (f) high–level cloud cover (CC), (g) precipitation, and (h) surface turbulent heat fluxes (STHF, upward is positive) over the central region for 21 March – 07 April 2022 derived from ERA5. For cloud cover, we show the median, the 25 and 75th percentiles, and the 5 and 95th percentiles of a 6 hour interval over open–water surfaces only as crosses, thick vertical lines, and thin vertical lines, respectively. In (g), we display area–averaged values of the accumulated 6 hour snowfall distinguished between convective and total precipitation, and open water (OW) and sea ice (SI). White crosses show the accumulated mean rainfall with more than $0.05\,\mathrm{mm}\,(6\,\mathrm{h})^{-1}$.

whether the environmental conditions C1–C6 (see Sect. 2.4.4) were fulfilled in a $200\,\mathrm{km}$ radius around the pressure minimum of the Polar Low at that time (Fig. 12):

The vertical temperature gradient conditions C1 and C2 are fulfilled with $44\,\mathrm{K}$ and $8.5\,\mathrm{K}$, respectively, while the lapse rate condition (C3) was not fulfilled with $4.2\,\mathrm{K\,km^{-1}}$. Conditions $C4_i$ and $C4_{ii}$, which are a measure for the availability of moisture for latent heat release, exceed the thresholds of $75\,\%$ and $82\,\%$ with $92.7\,\%$ and $93.9\,\%$. Near surface wind gusts reached $16.6\,\mathrm{m\,s^{-1}}$ during the development phase of the Polar Low (00 UTC) and increased to $18.8\,\mathrm{m\,s^{-1}}$ 9 hours later at the mature stage. In both stages, condition C5 was fulfilled. If we considered the maximum of the $10\,\mathrm{m}$ wind speed instead of the gust from ERA5, the condition would not have been fulfilled. However, using the Copernicus Arctic Regional Reanalysis (CARRA) from ECMWF with a $2.5\,\mathrm{km}{\times}2.5\,\mathrm{km}$ resolution, we found maximum wind speeds of more than $16\,\mathrm{m\,s^{-1}}$ ($19\,\mathrm{m\,s^{-1}}$) at 00 UTC (09 UTC). The trough connected to the Polar Low was not sufficiently strong with respect to the climatology as the geopotential height anomaly (C6) was only $-80\,\mathrm{gpm}$. Anomalously high geopotential around Svalbard and the central Arctic during that time might have obscured the strength of the trough, resulting in the failure of condition C6.

Some of the conditions had a large regional variability within the $200\,\mathrm{km}$ circle. Condition C2 ranged from below the threshold of $6\,\mathrm{K}$ in the southern part of the Polar Low to $10\,\mathrm{K}$ in the northern half. As the northwestern part of the circle lay over sea ice, the vertically averaged lower tropospheric lapse rate (C3) indicated stable stratification and reached values up to $10\,\mathrm{K\,km^{-1}}$. These high values of the lapse rate dominated the computation of the 75th percentile although the lapse rate was below the threshold in most parts of the circle.

At the mature stage (08 April 06–09 UTC), the region of maximum $\mathrm{SST}-\mathrm{T_{500\,hPa}}$ difference coincided well with the observed convective clouds during the research flight with HALO in the eastern part of the Polar Low (see Appendix E, Fig. E1). It also overlapped with the maximum precipitation rate ($1.2\,\mathrm{mm\,h^{-1}}$) and strongest updrafts (-$1.75\,\mathrm{Pa\,s^{-1}}$ at $850\,\mathrm{hPa}$) indicated by ERA5 (not shown). It is likely that higher precipitation rates and updrafts occurred that were smoothed out by the relatively coarse ERA5 data.

Dropsonde measurements between 06:55 and 07:53 UTC show high values of relative vorticity in the lowest $2\,\mathrm{km}$ and above $6\,\mathrm{km}$, indicating cyclonic rotation. When averaging ERA5 vorticity over the grid points closest to the dropsonde positions, we find a disagreement to the dropsonde measurements below and good agreement above $4\,\mathrm{km}$ height. While the lower tropospheric relative vorticity is related to the Polar Low, the upper tropospheric value is associated with the trough in the geopotential height. The disagreement between ERA5 and the dropsondes could be due to a misrepresentation of the Polar Low's wind field in the reanalysis or due to spatio–temporal mismatches of its position. Measured relative vorticity at $850\,\mathrm{hPa}$ ($1.5\,\mathrm{km}$ height) was about $3.5{\cdot}10^{-5}\,\mathrm{s^{-1}}$ and therefore did not exceed the threshold suggested by Stoll (2022) ($> 20{\cdot}10^{-5}\,\mathrm{s^{-1}}$). However, the flight track was not perfectly aligned with the Polar Low's centre but extended too far to the south and east where the mean sea level pressure isobars do not suggest a closed circulation (Fig. 13b). Negative relative vorticity to the east of the Polar Low, which is related to lee effects, also influenced the calculation from the dropsonde measurements. ERA5 data shows a maximum of $22{\cdot}10^{-5}\,\mathrm{s^{-1}}$ at $850\,\mathrm{hPa}$ within the Polar Low on 08 April at 09 UTC.

As soon as the Polar Low drifted over sea ice, it started to dissipate due to the loss of atmospheric instability and strongly reduced upward sensible and latent heat fluxes. The Polar Low observed during HALO–(AC)[3] fulfilled four of the six conditions

(see Table 1). However, Polar Lows can also form without fulfilling all conditions. Considering the climatology of Polar Lows in Zahn and von Storch (2008), which covers the years 1949–2005, our Polar Low was located unusually far in the north. Also

470   Radovan et al. (2019) investigated 33 Polar Lows with the Arctic System Reanalysis, of which 32 were centered further to the south than our case. Despite its northerly position, the 10 m wind speed of our Polar Low was larger than the average over the 33 Polar Lows investigated in their study.
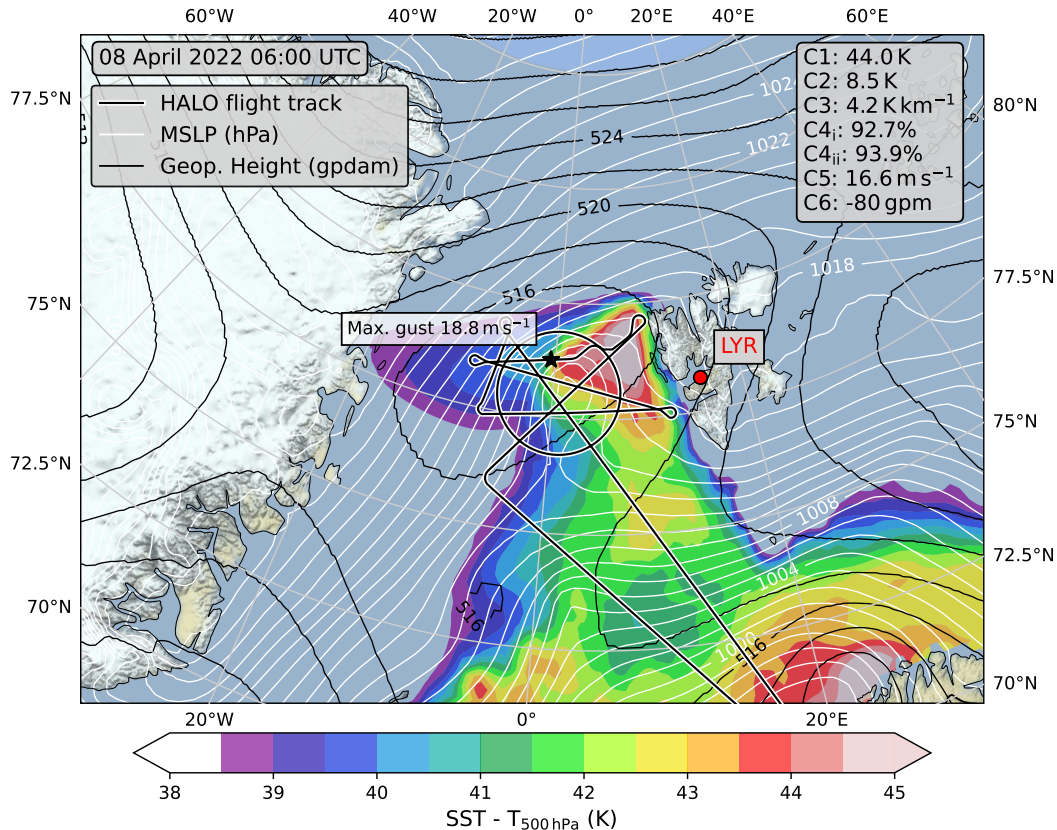
Figure 12. Mean sea level pressure (MSLP, white contour lines), 500 hPa geopotential height (black contour lines), and the difference between sea surface temperature (SST) and 500 hPa temperature during the mature stage of the Polar Low on 08 April 2022 06:00 UTC. Additionally, the maximum 10 m wind gust at 09:00 UTC (black star and text label) and the HALO flight track (black line with white outline) are included. The Polar Low conditions C1 ($SST - 500\,hPa$ temperature), C2 ($SST - T_{2\,m}$), C3 (vertical mean of the vertical potential temperature gradient below 850 hPa), C4 (i: mean relative humidity below 950 hPa, ii: mean relative humidity between 850 and 950 hPa), C5 (maximum 10 m wind speed), and C6 (500 hPa geopotential height anomaly) analysed by Radovan et al. (2019) are given for 08 April 2022 00:00 UTC. Data is based on ERA5.

Table 1. Criteria to evaluate environmental conditions of a Polar Low in a 200 km radius around its pressure minimum according to Radovan et al. (2019). An "X" in the right column indicates that the condition is fulfilled.

Condition	Meaning	How evaluated	Threshold	Fulfilled
C1	Sea surface temperature $-$ 500 hPa temperature	75th percentile	$\geq 43\,\text{K}$	X
C2	Sea surface temperature $-$ 2 m temperature	75th percentile	$\geq 6\,\text{K}$	X
C3	Mean lapse rate below 850 hPa	75th percentile	$\leq 3\,\text{K}\,\text{km}^{-1}$	
C4$_\text{i}$	Mean relative humidity below 950 hPa	75th percentile	$\geq 75\,\%$	X
C4$_\text{ii}$	Mean relative humidity between 850 and 950 hPa	75th percentile	$\geq 82\,\%$	X
C5	10 m wind gust	maximum	$\geq 15\,\text{m}\,\text{s}^{-1}$	X
C6	500 hPa geopotential height anomaly	mean	$\leq -160\,\text{gpm}$	
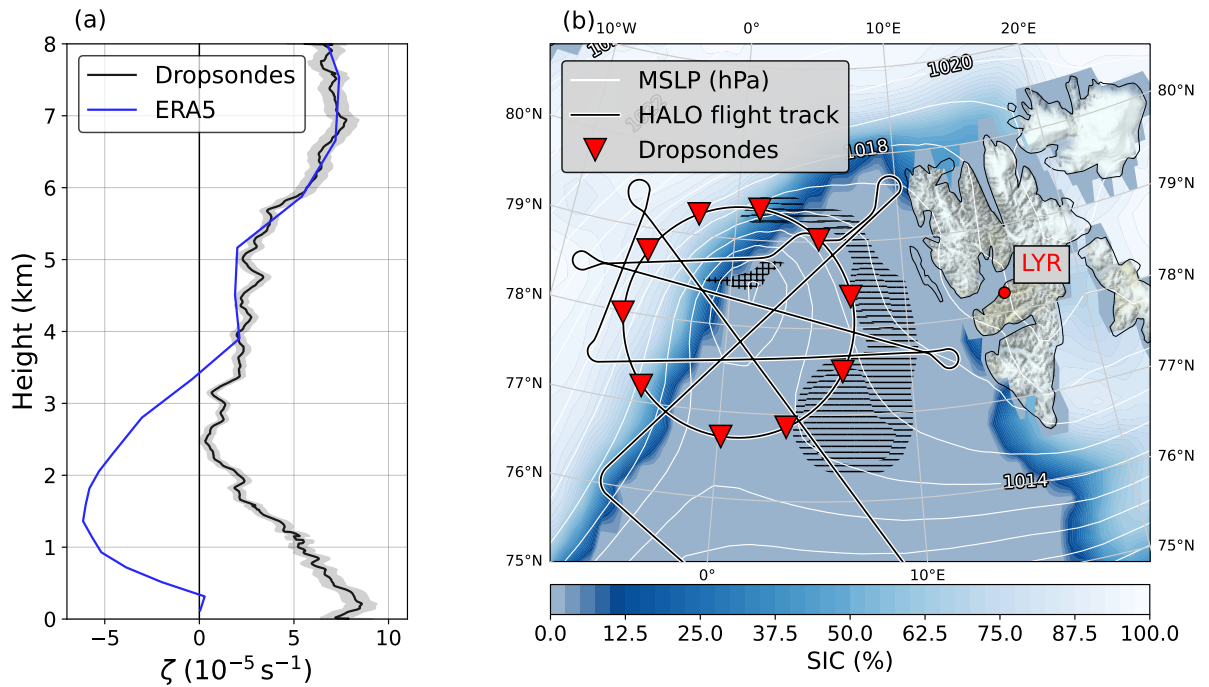
Figure 13. (a) Relative vorticity ζ computed from 10 dropsondes (black) and as model output from ERA5 averaged over the grid points nearest to the dropsondes (blue). (b) Location of the dropsondes (red triangles) launched from HALO while flying in a circle around the Polar Low. ERA5 based mean sea level pressure (white contour lines) and sea ice concentration (coloured filled contours) is shown for 08 April 2022 09 UTC. The HALO flight track is displayed as black line with white outline. Horizontal (horizontal and vertical) hatching indicates areas where ERA5 based 850 hPa relative vorticity is below $-10 \cdot 10^{-5}\,\text{s}^{-1}$ (above $20 \cdot 10^{-5}\,\text{s}^{-1}$).

4.4 Arctic cirrus over sea ice

The sequence of HALO flights between 10 – 12 April aimed to characterize a pronounced field of Arctic cirrus, which entered
the central Arctic through the Fram Strait and was finally located close to the North Pole. The initial synoptic state of this
period was dominated by a low pressure system, which was centered over Scandinavia on 09 April, advecting warm and moist
air westwards (see Sect. 3.1). Along approximately the $5°$ W meridian the westward flow converged with a cold air mass that
formed over the Greenland ice sheet and flowed eastwards into the Fram Strait. Due to the convergence, a strong vertical wind
shear developed south of Greenland with low–level northeasterly winds and southeasterly winds at levels above $700\,\mathrm{hPa}$ along
the east coast of Greenland. The southerly upper–level flow generated a poleward moisture transport, which was accompanied
by cirrus and mid–level clouds west of Svalbard and north of Greenland. This upper–level flow continued during the sequence
of three research flights conducted by HALO and roughly connected the air masses sampled during the three consecutive days.

The trajectories of the air masses sampled on 11–12 April are shown in Fig. 14a, c. While on 11 April two branches, one
southerly and one easterly, merged into the area of observations, the trajectories of 12 April first followed the westward moist
air transport south of Svalbard and then turned northwards into the central Arctic. Figure 14b and d illustrate the relative
humidity over ice from all dropsondes launched in the central Arctic during the HALO flights on 11–12 April. The mean
profile shows an enhanced moisture layer between $4\,\mathrm{km}$ and $8\,\mathrm{km}$. This layer is associated with higher wind speeds up to
$25\,\mathrm{m\,s^{-1}}$ and a shift in wind direction from an easterly flow in the lower $3\,\mathrm{km}$ to a southerly flow in the upper troposphere.
Below $4\,\mathrm{km}$ altitude, the air mass was rather dry with relative humidity below $50\,\%$. In these lower altitudes, the stable cold
and dry air mass in the central Arctic was supported by the outflow of cold and dry air from northern Greenland and prohibited
the formation of clouds below the cirrus. The airborne measurements during this constellation of isolated, widespread cirrus
over the sea ice in the central Arctic are well suited to investigate the evolution and radiative effect of Arctic cirrus over sea
ice, of which only few observations exist.

5 Conclusions

In this study, we described the weather and sea ice conditions during the HALO–(AC)[3] aircraft campaign carried out from 07
March to 12 April 2022 in the North Atlantic sector of the Arctic. The analysis is based on the ERA5 reanalysis, dropsondes,
satellite based sea ice products, and atmospheric measurements at Ny–Ålesund. We focus on three measurement regions of
the campaign: the sea ice covered Arctic Ocean north of Svalbard and Greenland (northern region), the Fram Strait (central
region), and the Greenland and Norwegian Seas between Svalbard and Scandinavia (southern region). The climatological
context is given with respect to the years 1979–2022.

Based on the vertically integrated meridional water vapour transport ($\mathrm{IVT_{north}}$) and the MCAO index M, the campaign was
separated into a warm period (11–20 March), and a cold period (21 March–12 April). During the warm (cold) phase, $\mathrm{IVT_{north}}$
was positive (negative) while M was negative (positive), respectively.

The warm period at the beginning of the campaign was characterized by a consistent southerly flow, which led to a strong
MWAI on 12–13 March that was detected as an Atmospheric River (AR) and reached the central Arctic. It was followed by an
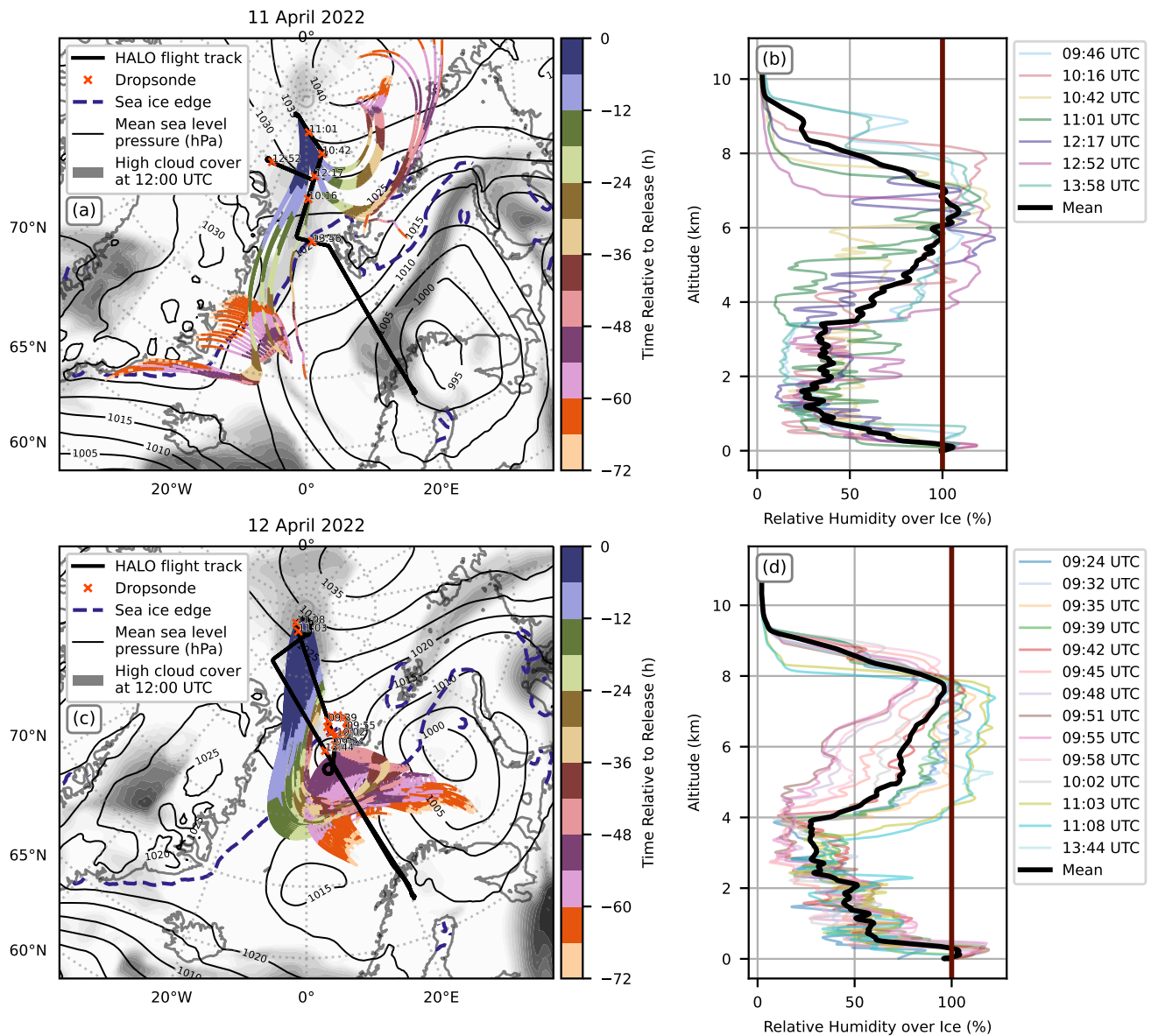
Figure 14. (a, c) Three day back trajectories of air masses in which cirrus were sampled on 11 and 12 April 2022. All trajectories are based on ERA5 reanalysis and end at the HALO flight track in cirrus level between 350 and 550 hPa. Surface pressure (thin black lines) and cloud cover (black shading) above 550 hPa from ERA5 are shown for 12 UTC at both days. The thick black line indicates the HALO flight track, and red crosses the location of dropsonde releases. In (b, d) we show the average profile and all individual profiles of relative humidity over ice measured during the two flights by dropsondes.

even stronger AR on 15–16 March. Compared to the climatology, both ARs denoted higher IVT and were centered further in the north than 75% (partly, 90%) of all ARs in the North Atlantic pathway within the ERA5 climatology. During the AR on 15–16 March, we found new maxima of vertically integrated meridional heat and water vapour fluxes (IHT$_{north}$ and IVT$_{north}$) for the central region latitudes. The radiosondes at Ny–Ålesund detected unusually high tropopause altitudes up to $12.9\,km$. Although the MWAIs were relatively short–lived, they caused a campaign average northward transport of heat and moisture, overcompensating the southward transport of the much longer cold period. We therefore stress the importance of MWAIs for the energy exchange between the mid–latitudes and the Arctic. Averaged over the warm period, new maximum rainfall rates were found over the sea ice northwest of Svalbard, exceeding the climatology by a factor of 36. Not only is the intensity remarkable, but also the occurrence of rain over sea ice at this time of the year.

The cold period was initialized after the passage of a strong cyclone over Svalbard on 21 March, when a northerly flow was established in the central region. We identified two strong MCAO periods (21–26 March and 01–02 April), where M partly exceeded the 90th percentile. The strong MCAOs were associated with high upward fluxes of sensible and latent heat in the unstable atmospheric boundary layer, which stress the interaction between the warm ocean and cold atmosphere. The ocean–atmosphere interactions in the boundary layer resulted in the typical high fraction of low–level cloud cover (cloud streets) and convective precipitation. After each strong MCAO period, aged warm air was advected to the measurement regions by a weaker northeasterly flow. During the aged warm air period, precipitation faded in the central region due to warming and drying. West of Svalbard, cloud–free conditions prevailed because of orographic lee effects (foehn).

After a weak MCAO, a Polar Low formed in the Fram Strait on 07 April. We confirmed that four out of six criteria for Polar Low development were fulfilled by inspecting the environmental conditions. With the help of dropsondes launched along a circle, we found strong rotation confined to the lowest $2\,km$ despite negative relative vorticity in the eastern part related to lee effects. The Polar Low was located unusually far in the north. At the end of the cold period (10–12 April), warm and moist air was advected by a Scandinavian Low towards the southern region and diverted northwards through the Fram Strait. The high altitude southerly winds transported cirrus clouds over the sea ice with cold and dry air from the Greenland ice sheet below. This combination resulted in an isolated humidity layer including Arctic cirrus in the absence of low– and mid–level clouds.

With respect to the climatology, the entire campaign was slightly warmer considering both $2\,m$ and $850\,hPa$ temperatures, except for the central Fram Strait and north of Greenland. Here, $2\,m$ temperature anomalies were negative. In the central region, SICs were within the 10–90th percentiles of the climatology during the entire campaign period. The AR events caused remarkable reductions of SIC in the Fram Strait and northeast of Svalbard due to dynamical forcing by wind and ocean, and possibly melt. Afterwards during the MCAO period, temperatures stayed below the freezing point and northerly winds increased SIC above the climatological mean in those regions. Only around Svalbard and at its southeastern coast, SICs were lower than the climatological mean values. We identified a strip of positive SIC anomaly in the central and western Fram Strait, which coincides well with negative $2\,m$ temperature anomalies.

Atmospheric soundings and near–surface measurements at Ny–Ålesund generally represent the weather conditions of the central region well, when respecting the temporal delay of up to 1 day due to the propagation of synoptic systems during the warm period. However, during the cold period, lee effects at the coast of Svalbard cause cloud conditions that are only

representative for the eastern part of the central region. The additional measurements at the AWIPEV can be implemented into the data analysis of HALO–(AC)[3] and provide a long–term climatological context to the airborne measurements.

Compared to previous aircraft campaigns in the Arctic within (AC)[3] that focused on the evolution of (mixed–phase) clouds (ACLOUD; AFLUX and MOSAiC–ACA, Wendisch et al., 2019; Mech et al., 2022), we observed a larger variety of MCAO conditions during HALO–(AC)[3]. The long phase of MCAOs with varying strength and different wind regimes provides opportunities for detailed MCAO studies making use of the airborne measurements. Also the sea ice edge was closer to Svalbard than during AFLUX (March–April 2019) so that ocean–ice transects could be performed more easily. We captured several MWAIs / ARs with unusual or even record breaking strength. With regard to the changing climate when exchanges between the mid–latitudes and the Arctic become more frequent and ARs are expected to shift poleward, the campaign provides a unique opportunity to study stronger than average MWAIs / ARs. We conclude that the weather conditions were well suited to achieve the objectives of the HALO–(AC)[3] campaign.

Code and data availability. All codes used for the analyses presented in this study have been uploaded to GITHUB and connected with ZENODO for public access (*in preparation*). Sea ice concentration climatology data is found on OSI SAF (2017) and Copernicus Climate Change Service (C3S) (2020). The high resolution sea ice concentration dataset used for 07 March–12 April 2022 is based on the product from the Institute of Environmental Physics, University of Bremen. The data is available at https://seaice.uni-bremen.de/data/modis_amsr2. ERA5 data on single and pressure levels can be accessed through Hersbach et al. (2018b) and Hersbach et al. (2018a). Ny–Ålesund radiosondes and ceilometer data have been published on PANGAEA (Maturilli and Kayser, 2016, 2017; Maturilli, 2020b, 2022). Near–surface meteorology data from Ny–Ålesund is available on PANGAEA as well (Maturilli, 2020a). Dropsonde data from used in this study can be found on ZENODO (*in preparation*).

Table A1. Geographical coordinates for measurement regions as displayed in Fig. 1. Note that the northern part of the northern region in the central Arctic is extended to the west.

	Northern region	Northern region extension	Central region	Southern region
Northern limit in deg N	84.5	89.3	81.5	75.0
Southern limit in deg N	81.5	84.5	75.0	70.6
Western limit in deg E	-9.0	-54.0	-9.0	0.0
Eastern limit in deg E	30.0	30.0	16.0	23.0

Appendix A: Methodology details

This part of the appendix includes additional details regarding the methods described in Sect. 2 that go beyond the necessary information to understand the study but help to reproduce the results.

For an exact computation of the regional averages over the southern, central and northern regions, we provide the geographical coordinates of the domains' boundaries in Table A1.

Here, we describe the processing of variables to analyse the MCAO conditions (Sect. 2.4.3) in greater detail for reproducibility. Turbulent flux data was confined to open water surfaces because our focus is on the intensity of the upward fluxes (positive sign) over open water during the MCAOs. We used the mean values over 1 hour at each grid point instead of the instantaneous values (Hersbach et al., 2020). For low, medium and high–level cloud cover, we computed the median value including 5, 25, 75, and 95th percentiles. Precipitation data was accumulated over 6 hour intervals and grouped into open water and sea ice covered surfaces. Snowfall is further separated into its large–scale and convective parts. The latter is defined in ERA5 as the frozen precipitation resulting from the convection scheme and thus from subgrid–scale convection. Total precipitation is then the sum of the convective and the large–scale part (Hersbach et al., 2020).

In the following, we summarize the meanings of the conditions tested for Polar Low formation (Sect. 2.4.4) for better understanding: Condition C1 is a measure of the convection potential as it evaluates the mean temperature gradient between the surface and the mid–troposphere. Large differences between the $2\,\mathrm{m}$ temperature and the SST (C2) promote strong sensible heat fluxes, stressing the air–sea interaction. Positive values of C3 represent an increase of potential temperature with height. At least conditionally unstable conditions (unstable (stable) for moisture–saturated (unsaturated) air parcels) should be present (C3 $\leq 3\,\mathrm{K\,km^{-1}}$). The relative humidity conditions $C4_\mathrm{i}$ and $C4_\mathrm{ii}$ are an important measure for the availability of moisture for latent heat release, a major energy source of a Polar Low. Maximum $10\,\mathrm{m}$ wind speed (C5) is an indicator of the Polar Low's strength. The geopotential height condition (C6) is selected to ensure the presence of an upper level trough.

Appendix B: Integrated water vapour transport for moist and warm air intrusions

For the MWAIs / ARs on 13 and 15 March, and for the weaker MWAI on 10 April, we show the total IVT in Fig. B1. While the former two events were meridionally aligned, the latter had a rather zonal orientation. The strongest total IVT is found on 15 March, exceeding $400\,\mathrm{kg\,m^{-1}\,s^{-1}}$.
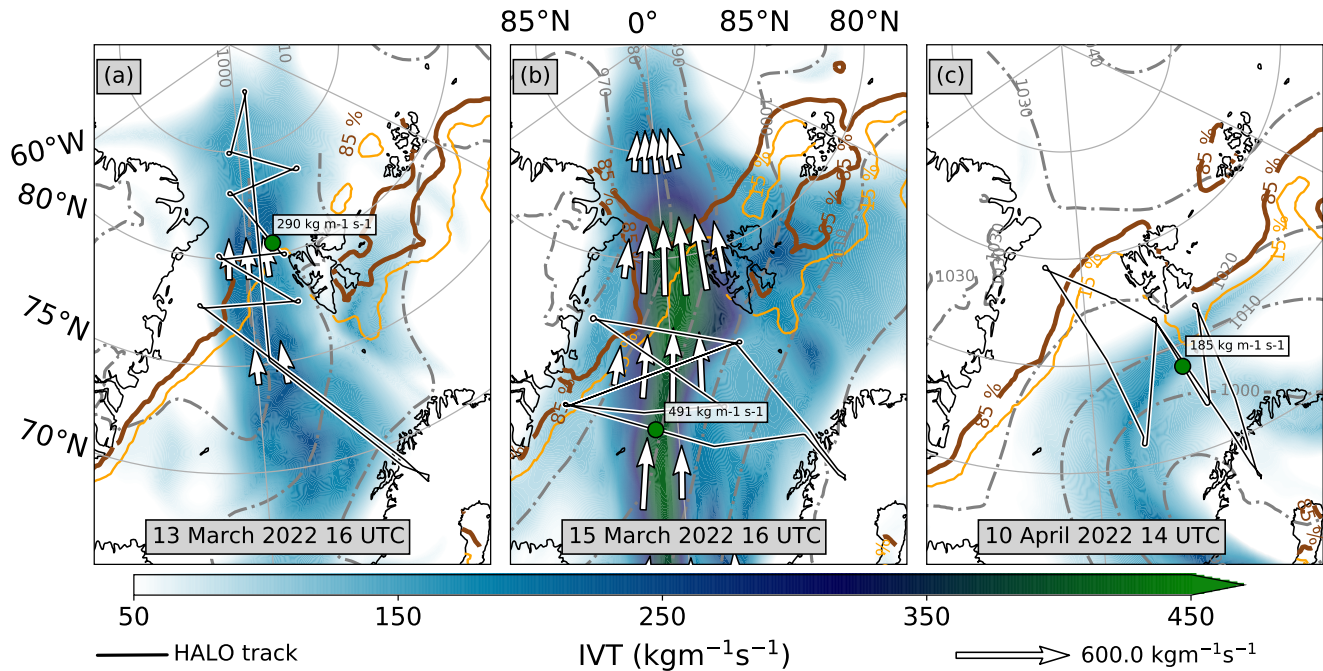
Figure B1. Total integrated water vapour transport (IVT, zonal and meridional component) from ERA5 (colours) and dropsondes (circular marker) for three moist and warm air intrusions / Atmospheric Rivers: (a) 13 March 2022 16 UTC, (b) 15 March 2022 16 UTC, (c) 10 April 2022 14 UTC. Quivers indicating the flow direction and strength, as well as the HALO flight track (black line with white outline) are also included. The orange (brown) line indicate the 15 % (85 %) sea ice concentration isoline. Grey dash–dotted contours show the mean sea level pressure. Data is based on ERA5.

 Appendix C: Moist and warm air intrusion trajectories

The general air flow on two selected MWAI / AR days is investigated. Three day back and two day forward trajectories shown in Fig. C1 are initialized on 13 and 15 March each at 18:00 UTC. The trajectories reveal that the air masses of the first MWAI day mainly originated from central Europe and the second case from the North Atlantic. Forward trajectories show that both MWAIs / ARs reached the central Arctic.
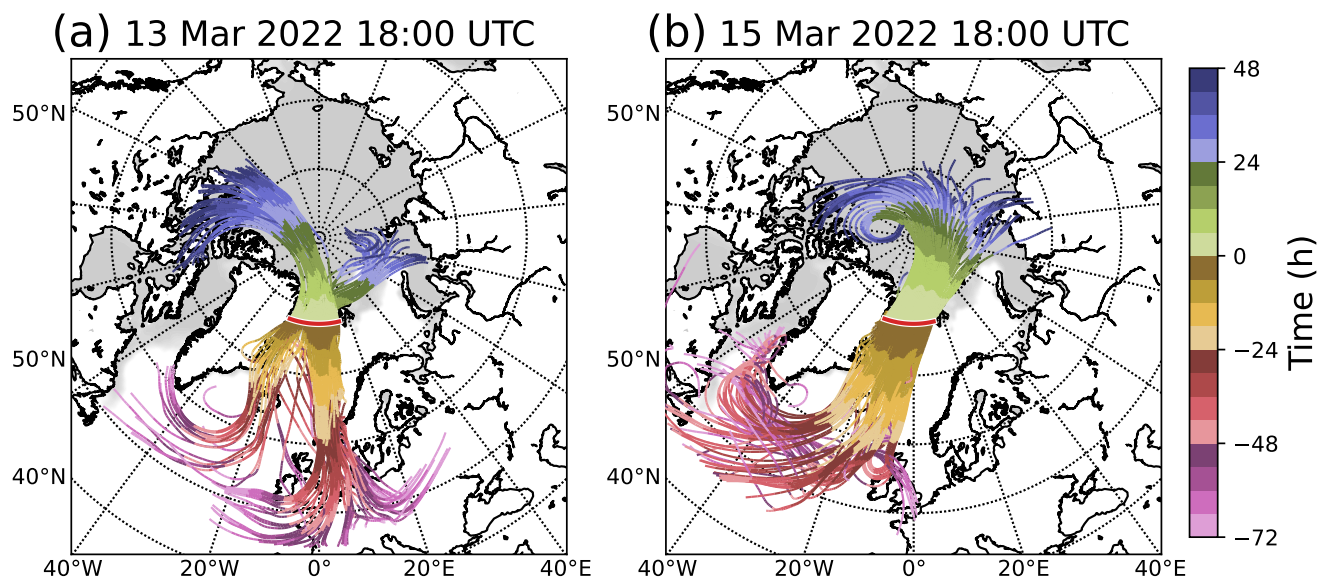
Figure C1. Three day backward and two day forward trajectories of the AR air masses observed in the central region on (a) 13 March 2022 18:00 UTC, and (b) 15 March 2022 18:00 UTC. at altitudes of 700, 850, and 925 hPa. Starting points are placed at 77.5° N between 20° W and 13° E with a zonal spacing of 1°. Both 72 hour back–trajectories as well as 48 hour forward–trajectories are computed. Grey shading indicates the sea ice concentration from ERA5.

 Appendix D: Marine cold air outbreak

Figure D1 shows the ERA5 based temporal evolution of temperature, relative humidity and wind for the eastern part of the northern region (identical western longitude boundary as the central region). The data has been processed as described in Sect. 2.4.3 and Appendix A. During the stronger MCAOs in the central region with northerly winds, the air masses originated from the northern region. Due to the low occurrence of northwesterly winds, the western extension of the northern region is not included. For comparison of turbulent fluxes between the central and southern region, we include Fig. D2.
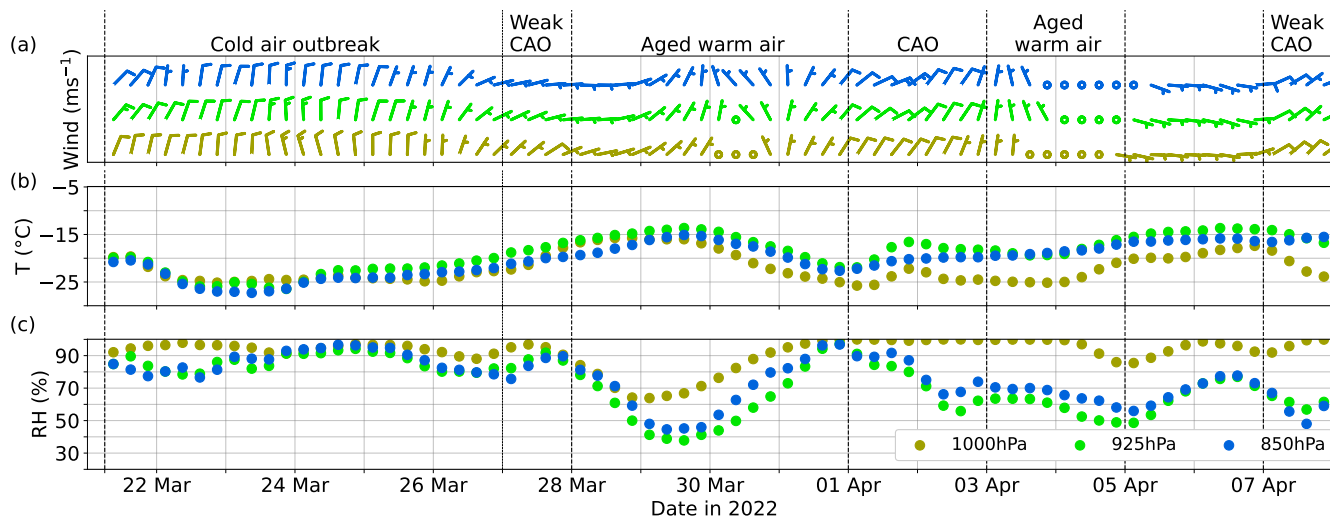
Figure D1. Temporal evolution of (a) wind, (b) air temperature (T), and (c) relative humidity (RH) on the 1000, 925, and 850 hPa pressure levels as in Fig. 11, but for the northern region (without western extension). Data is based on ERA5.
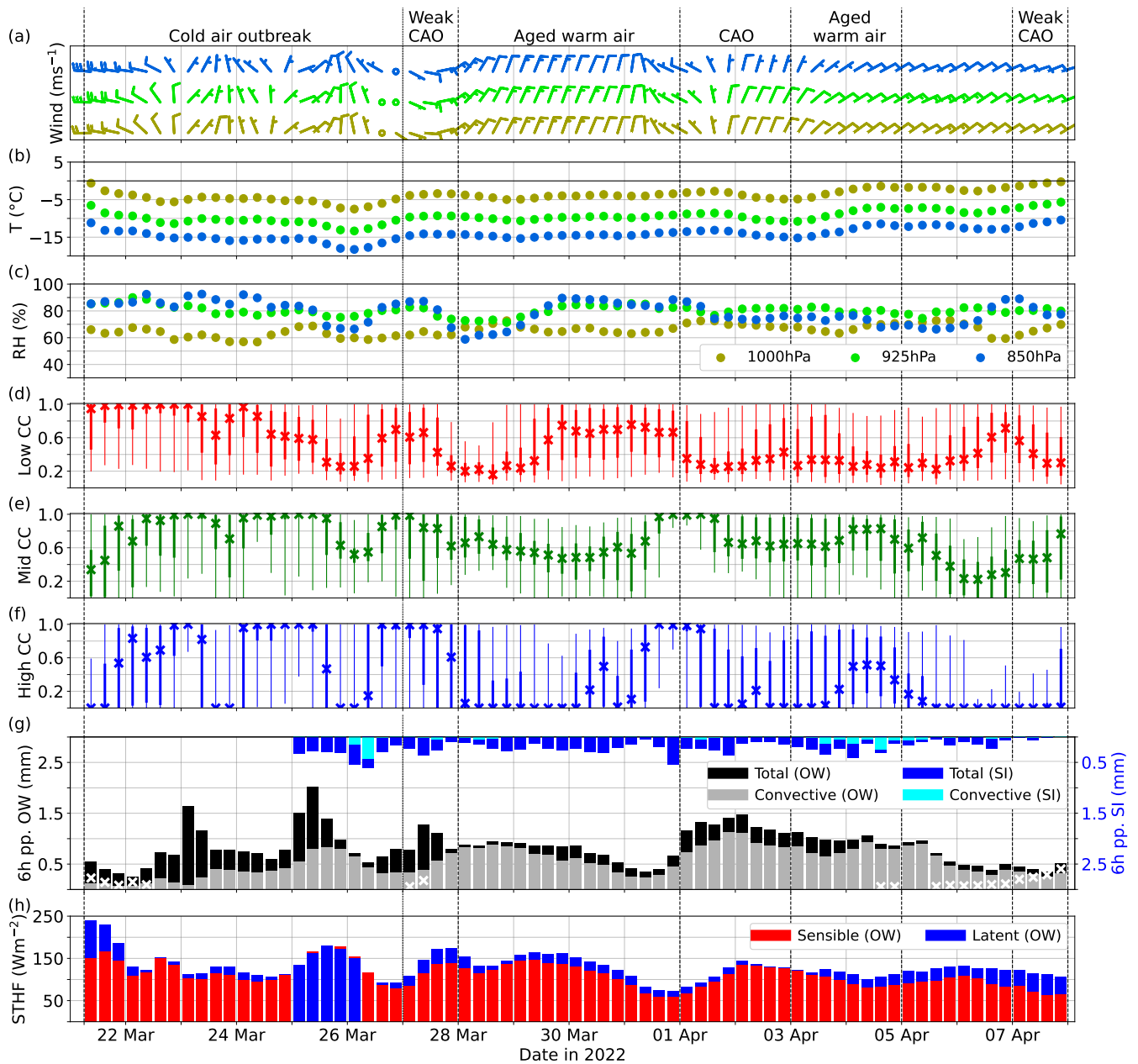
Figure D2. Temporal evolution of (a) wind, (b) air temperature (T), and (c) relative humidity (RH) on the 1000, 925, and 850 hPa pressure levels, and of (d) low–, (e) mid–, and (f) high–level cloud cover (CC), (g) precipitation, and (h) surface turbulent heat fluxes (STHF) as in Fig. 11 but for the southern region. Data is based on ERA5.

Appendix E: Polar Low visual observations

Due to the relatively small extent of a Polar Low, we were able to see the entire structure during the HALO research flight on 08 April 2022. The photo was taken on one of the cross sections through the Polar Low, showing the relatively cloud free centre (eye) and the convective cloud band on its (north–)eastern side (Fig. E1).
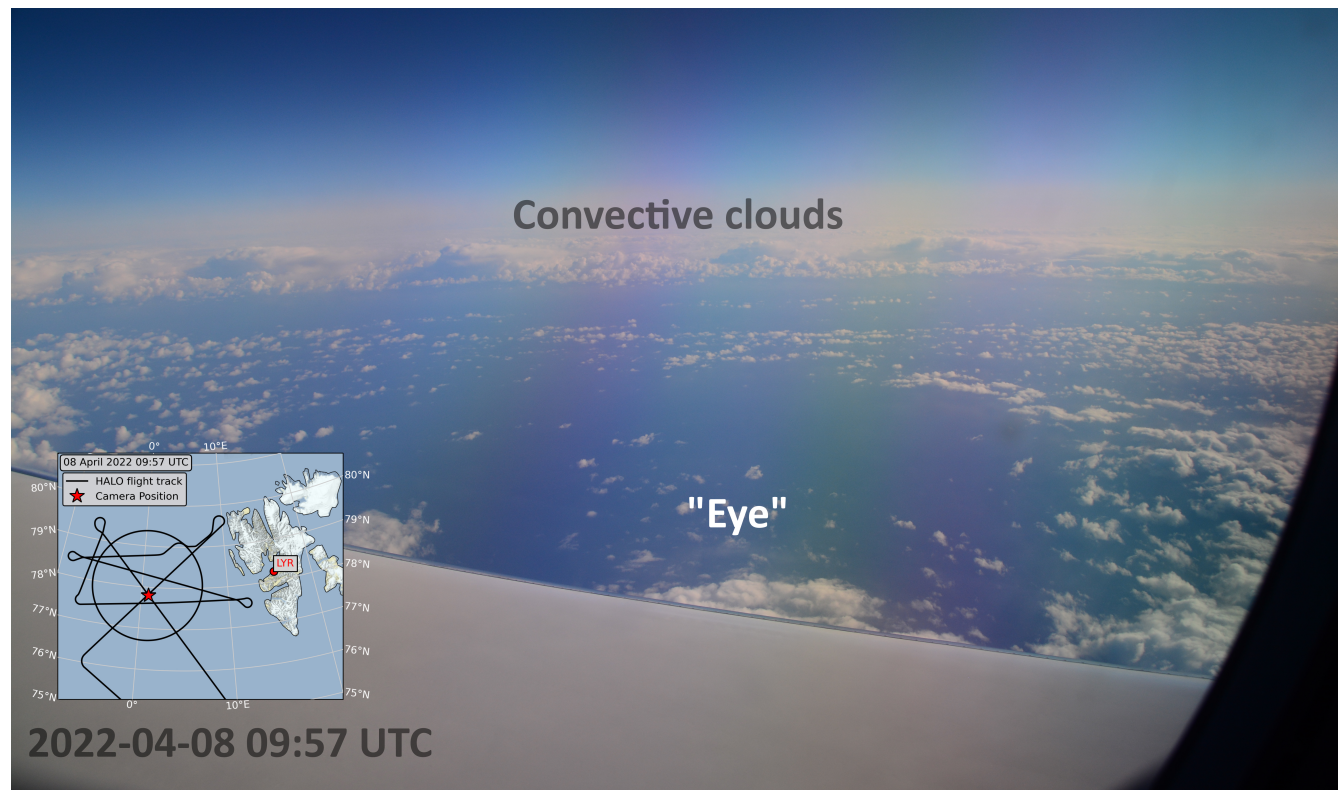
Figure E1. Photo of the Polar Low taken from HALO (portside) on 08 April 2022 at 09:57 UTC. The centre (eye) of the Polar Low can be seen in the foreground while the convective cloud band is visible in the background. The map indicates the flight track (black line) and the position of the aircraft at that time (red star). © Andreas Walbröl

600 *Author contributions.* SC, AE, IG, JanM, MW, and AW conceptualized the manuscript. MW and AW formulated the introduction with comments and input from AE, JanM, and SC. HD, BK, ML, NM, MM, JanR, and AW prepared the description of the data and methods chapter. SB, HD, BK, ML, JanM, HM, RN, FP, JohR, JanR, IS, NS, and AW provided visualisations and analysed figures. JohM and AW collected codes from co–authors and made them publicly available. AW is the main author of this manuscript and ensured validation. All co–authors reviewed the manuscript.

605   *Competing interests.*   The authors declare that they have no conflict of interest.

Acknowledgements.   We gratefully acknowledge the funding by the Deutsche Forschungsgemeinschaft (DFG, German Research Foundation) for the ArctiC Amplification: Climate Relevant Atmospheric and SurfaCe Processes, and Feedback Mechanisms (AC)[3] Project Number 268020496 – TRR 172 within the Transregional Collaborative Research Center. We are further grateful for funding of project grant no. 316646266 by the Deutsche Forschungsgemeinschaft (DFG, German Research Foundation) within the framework of Priority Programme
610   SPP 1294 to promote research with HALO. We thank the Institute of Environmental Physics, University of Bremen for the provision of the merged MODIS-AMSR2 sea–ice concentration data at https://seaice.uni-bremen.de/data/modis_amsr2 (last access 2023-04-04). Hersbach et al. (2018a) and Hersbach et al. (2018b) were downloaded from the Copernicus Climate Change Service (C3S) Climate Data Store. The results contain modified Copernicus Climate Change Service information 2022. Neither the European Commission nor ECMWF is responsible for any use that may be made of the Copernicus information or data it contains. We thank the Alfred Wegener Institute for
615   providing and operating the two aircraft (Polar 5 and Polar 6), the crew, and also the technicians of the Polar 5 and Polar 6 aircraft. We are also grateful for the research aircraft HALO, the pilots and technicians provided and operated by the German Aerospace Centre (Deutsches Zentrum für Luft– und Raumfahrt).

References

Avila-Diaz, A., Bromwich, D. H., Wilson, A. B., Justino, F., and Wang, S.-H.: Climate Extremes across the North American Arctic in Modern Reanalyses, J. Climate, 34, 2385–2410, https://doi.org/10.1175/JCLI-D-20-0093.1, 2021.

Bony, S. and Stevens, B.: Measuring Area-Averaged Vertical Motions with Dropsondes, J. Atmos. Sci., 76, 767–783, https://doi.org/10.1175/JAS-D-18-0141.1, 2019.

Bresson, H., Rinke, A., Mech, M., Reinert, D., Schemann, V., Ebell, K., Maturilli, M., Viceto, C., Gorodetskaya, I., and Crewell, S.: Case study of a moisture intrusion over the Arctic with the ICOsahedral Non-hydrostatic (ICON) model: resolution dependence of its representation, Atmos. Chem. Phys., 22, 173–196, https://doi.org/10.5194/acp-22-173-2022, 2022.

Cohen, J., Zhang, X., Francis, J., Jung, T., Kwok, R., Overland, J., Ballinger, T. J., Bhatt, U. S., Chen, H. W., Coumou, D., Feldstein, S., Gu, H., Handorf, D., Henderson, G., Ionita, M., Kretschmer, M., Laliberte, F., Lee, S., Linderholm, H. W., Maslowski, W., Peings, Y., Pfeiffer, K., Rigor, I., Semmler, T., Stroeve, J., Taylor, P. C., Vavrus, S., Vihma, T., Wang, S., Wendisch, M., Wu, Y., and Yoon, J.: Divergent consensuses on Arctic amplification influence on midlatitude severe winter weather, Nat. Clim. Change, 10, 20–29, https://doi.org/10.1038/s41558-019-0662-y, 2020.

Copernicus Climate Change Service (C3S): Sea ice concentration daily gridded data from 1979 to present derived from satellite observations, Copernicus Climate Change Service (C3S) Climate Data Store (CDS) [data set], https://doi.org/10.24381/CDS.3CD8B812, 2020.

Dahlke, S., Solbès, A., and Maturilli, M.: Cold Air Outbreaks in Fram Strait: Climatology, Trends, and Observations During an Extreme Season in 2020, J. Geophys. Res.: Atmos., 127, https://doi.org/10.1029/2021JD035741, 2022.

Di Biagio, C., Pelon, J., Blanchard, Y., Loyer, L., Hudson, S. R., Walden, V. P., Raut, J., Kato, S., Mariage, V., and Granskog, M. A.: Toward a Better Surface Radiation Budget Analysis Over Sea Ice in the High Arctic Ocean: A Comparative Study Between Satellite, Reanalysis, and local-scale Observations, J. Geophys. Res.: Atmos., 126, https://doi.org/10.1029/2020JD032555, 2021.

Drüe, C. and Heinemann, G.: High-resolution maps of the sea-ice concentration from MODIS satellite data, Geophys. Res. Lett., 31, L20 403, https://doi.org/10.1029/2004GL020808, 2004.

Fletcher, J., Mason, S., and Jakob, C.: The Climatology, Meteorology, and Boundary Layer Structure of Marine Cold Air Outbreaks in Both Hemispheres*, J. Climate, 29, 1999–2014, https://doi.org/10.1175/JCLI-D-15-0268.1, 2016.

Francis, J. A. and Vavrus, S. J.: Evidence for a wavier jet stream in response to rapid Arctic warming, Environ. Res. Lett., 10, 014 005, https://doi.org/10.1088/1748-9326/10/1/014005, 2015.

George, G., Stevens, B., Bony, S., Pincus, R., Fairall, C., Schulz, H., Kölling, T., Kalen, Q. T., Klingebiel, M., Konow, H., Lundry, A., Prange, M., and Radtke, J.: JOANNE: Joint dropsonde Observations of the Atmosphere in tropical North atlaNtic meso-scale Environments, Earth Syst. Sci. Data, 13, 5253–5272, https://doi.org/10.5194/essd-13-5253-2021, 2021.

Graham, R. M., Cohen, L., Ritzhaupt, N., Segger, B., Graversen, R. G., Rinke, A., Walden, V. P., Granskog, M. A., and Hudson, S. R.: Evaluation of Six Atmospheric Reanalyses over Arctic Sea Ice from Winter to Early Summer, J. Climate, 32, 4121–4143, https://doi.org/10.1175/JCLI-D-18-0643.1, 2019a.

Graham, R. M., Hudson, S. R., and Maturilli, M.: Improved Performance of ERA5 in Arctic Gateway Relative to Four Global Atmospheric Reanalyses, Geophys. Res. Lett., 46, 6138–6147, https://doi.org/10.1029/2019GL082781, 2019b.

Guan, B. and Waliser, D. E.: Detection of atmospheric rivers: Evaluation and application of an algorithm for global studies: Detection of Atmospheric Rivers, J. Geophys. Res.: Atmos., 120, 12 514–12 535, https://doi.org/10.1002/2015JD024257, 2015.

Guan, B. and Waliser, D. E.: Atmospheric rivers in 20 year weather and climate simulations: A multimodel, global evaluation, J. Geophys. Res.: Atmos., 122, 5556–5581, https://doi.org/10.1002/2016JD026174, 2017.

Guan, B., Waliser, D. E., and Ralph, F. M.: An Intercomparison between Reanalysis and Dropsonde Observations of the Total Water Vapor Transport in Individual Atmospheric Rivers, J. Hydrometeorol., 19, 321–337, https://doi.org/10.1175/JHM-D-17-0114.1, 2018.

Hartmann, J., Kottmeier, C., and Raasch, S.: Roll Vortices and Boundary-Layer Development during a Cold Air Outbreak, Boundary Layer Meteorol., 84, 45–65, https://doi.org/10.1023/A:1000392931768, 1997.

Hersbach, H., Bell, B., Berrisford, P., Biavati, G., Horányi, A., Muñoz Sabater, J., Nicolas, J., Peubey, C., Radu, R., Rozum, I., Schepers, D., Simmons, A., Soci, C., Dee, D., and Thépaut, J.-N.: ERA5 hourly data on pressure levels from 1959 to present, Copernicus Climate Change Service (C3S) Climate Data Store (CDS) [data set], https://doi.org/10.24381/cds.bd0915c6, 2018a.

Hersbach, H., Bell, B., Berrisford, P., Biavati, G., Horányi, A., Muñoz Sabater, J., Nicolas, J., Peubey, C., Radu, R., Rozum, I., Schepers, D., Simmons, A., Soci, C., Dee, D., and Thépaut, J.-N.: ERA5 hourly data on single levels from 1959 to present, Copernicus Climate Change Service (C3S) Climate Data Store (CDS) [data set], https://doi.org/10.24381/cds.adbb2d47, 2018b.

Hersbach, H., Bell, B., Berrisford, P., Hirahara, S., Horányi, A., Muñoz-Sabater, J., Nicolas, J., Peubey, C., Radu, R., Schepers, D., Simmons, A., Soci, C., Abdalla, S., Abellan, X., Balsamo, G., Bechtold, P., Biavati, G., Bidlot, J., Bonavita, M., Chiara, G., Dahlgren, P., Dee, D., Diamantakis, M., Dragani, R., Flemming, J., Forbes, R., Fuentes, M., Geer, A., Haimberger, L., Healy, S., Hogan, R. J., Hólm, E., Janisková, M., Keeley, S., Laloyaux, P., Lopez, P., Lupu, C., Radnoti, G., Rosnay, P., Rozum, I., Vamborg, F., Villaume, S., and Thépaut, J.: The ERA5 global reanalysis, Q. J. R. Meteorolog. Soc., 146, 1999–2049, https://doi.org/10.1002/qj.3803, 2020.

Hock, T. F. and Franklin, J. L.: The NCAR GPS Dropwindsonde, Bull. Am. Meteorol. Soc., 80, 407–420, https://doi.org/10.1175/1520-0477(1999)080<0407:TNGD>2.0.CO;2, 1999.

Hong, Y. and Liu, G.: The Characteristics of Ice Cloud Properties Derived from CloudSat and CALIPSO Measurements, J. Climate, 28, 3880–3901, https://doi.org/10.1175/JCLI-D-14-00666.1, 2015.

Johansson, E., Devasthale, A., Tjernström, M., Ekman, A. M. L., and L'Ecuyer, T.: Response of the lower troposphere to moisture intrusions into the Arctic, Geophys. Res. Lett., 44, 2527–2536, https://doi.org/10.1002/2017GL072687, 2017.

Kapsch, M.-L., Graversen, R. G., and Tjernström, M.: Springtime atmospheric energy transport and the control of Arctic summer sea-ice extent, Nat. Clim. Change, 3, 744–748, https://doi.org/10.1038/nclimate1884, 2013.

Kapsch, M.-L., Skific, N., Graversen, R. G., Tjernström, M., and Francis, J. A.: Summers with low Arctic sea ice linked to persistence of spring atmospheric circulation patterns, Clim. Dyn., 52, 2497–2512, https://doi.org/10.1007/s00382-018-4279-z, 2019.

Kolstad, E. W., Bracegirdle, T. J., and Seierstad, I. A.: Marine cold-air outbreaks in the North Atlantic: temporal distribution and associations with large-scale atmospheric circulation, Clim. Dyn., 33, 187–197, https://doi.org/10.1007/s00382-008-0431-5, 2009.

Komatsu, K. K., Alexeev, V. A., Repina, I. A., and Tachibana, Y.: Poleward upgliding Siberian atmospheric rivers over sea ice heat up Arctic upper air, Sci. Rep., 8, 2872, https://doi.org/10.1038/s41598-018-21159-6, 2018.

Konow, H., Ewald, F., George, G., Jacob, M., Klingebiel, M., Kölling, T., Luebke, A. E., Mieslinger, T., Pörtge, V., Radtke, J., Schäfer, M., Schulz, H., Vogel, R., Wirth, M., Bony, S., Crewell, S., Ehrlich, A., Forster, L., Giez, A., Gödde, F., Groß, S., Gutleben, M., Hagen, M., Hirsch, L., Jansen, F., Lang, T., Mayer, B., Mech, M., Prange, M., Schnitt, S., Vial, J., Walbröl, A., Wendisch, M., Wolf, K., Zinner, T., Zöger, M., Ament, F., and Stevens, B.: EUREC[4]A's HALO, Earth Syst. Sci. Data, 13, 5545–5563, https://doi.org/10.5194/essd-13-5545-2021, 2021.

Lauer, M., Rinke, A., Gorodetskaya, I, Sprenger, M., Mech, M., and Crewell, S.: Influence of atmospheric rivers and associated weather systems on precipitation in the Arctic, Atmos. Chem. Phys. [preprint], https://doi.org/10.5194/egusphere-2023-261, 2023-06-16, 2023.

Lavergne, T., Sørensen, A. M., Kern, S., Tonboe, R., Notz, D., Aaboe, S., Bell, L., Dybkjær, G., Eastwood, S., Gabarro, C., Heygster, G., Killie, M. A., Brandt Kreiner, M., Lavelle, J., Saldo, R., Sandven, S., and Pedersen, L. T.: Version 2 of the EUMETSAT OSI SAF and ESA CCI sea-ice concentration climate data records, The Cryosphere, 13, 49–78, https://doi.org/10.5194/tc-13-49-2019, 2019.

695 Lee, S. H., Williams, P. D., and Frame, T. H. A.: Increased shear in the North Atlantic upper-level jet stream over the past four decades, Nature, 572, 639–642, https://doi.org/10.1038/s41586-019-1465-z, 2019.

Lenschow, D. H., Savic-Jovcic, V., and Stevens, B.: Divergence and Vorticity from Aircraft Air Motion Measurements, J. Atmos. Oceanic Technol., 24, 2062–2072, https://doi.org/10.1175/2007JTECHA940.1, 2007.

Ludwig, V., Spreen, G., and Pedersen, L. T.: Evaluation of a New Merged Sea-Ice Concentration Dataset at 1 km Resolution from Thermal 700 Infrared and Passive Microwave Satellite Data in the Arctic, Remote Sens., 12, 3183, https://doi.org/10.3390/rs12193183, 2020.

Ma, W., Chen, G., and Guan, B.: Poleward Shift of Atmospheric Rivers in the Southern Hemisphere in Recent Decades, Geophys. Res. Lett., 47, https://doi.org/10.1029/2020GL089934, 2020.

Marsing, A., Meerkötter, R., Heller, R., Kaufmann, S., Jurkat-Witschas, T., Krämer, M., Rolf, C., and Voigt, C.: Investigating the radiative effect of Arctic cirrus measured in situ during the winter 2015–2016, Atmos. Chem. Phys., 23, 587–609, https://doi.org/10.5194/acp-23-705 587-2023, 2023.

Mattingly, K. S., Mote, T. L., and Fettweis, X.: Atmospheric River Impacts on Greenland Ice Sheet Surface Mass Balance, J. Geophys. Res.: Atmos., 123, 8538–8560, https://doi.org/10.1029/2018JD028714, 2018.

Mattingly, K. S., Mote, T. L., Fettweis, X., van As, D., Van Tricht, K., Lhermitte, S., Pettersen, C., and Fausto, R. S.: Strong Summer Atmospheric Rivers Trigger Greenland Ice Sheet Melt through Spatially Varying Surface Energy Balance and Cloud Regimes, J. Climate, 710 33, 6809–6832, https://doi.org/10.1175/JCLI-D-19-0835.1, 2020.

Maturilli, M.: Continuous meteorological observations at station Ny-Ålesund (2011-08 et seq), https://doi.org/10.1594/PANGAEA.914979, 2020a.

Maturilli, M.: High resolution radiosonde measurements from station Ny-Ålesund (2017-04 et seq), PANGAEA - Data Publisher for Earth & Environmental Science [data set], https://doi.org/10.1594/PANGAEA.914973, 2020b.

715 Maturilli, M.: Ceilometer cloud base height from station Ny-Ålesund (2017-08 et seq), PANGAEA - Data Publisher for Earth & Environmental Science [data set], https://doi.org/10.1594/PANGAEA.942331, 2022.

Maturilli, M. and Ebell, K.: Twenty-five years of cloud base height measurements by ceilometer in Ny-Ålesund, Svalbard, Earth Syst. Sci. Data, 10, 1451–1456, https://doi.org/10.5194/essd-10-1451-2018, 2018.

Maturilli, M. and Kayser, M.: Homogenized radiosonde record at station Ny-Ålesund, Spitsbergen, 1993-2014, PANGAEA - Data Publisher 720 for Earth & Environmental Science [data set], https://doi.org/10.1594/PANGAEA.845373, 2016.

Maturilli, M. and Kayser, M.: Homogenized radiosonde record at station Ny-Ålesund, Spitsbergen, 2015-2016, PANGAEA - Data Publisher for Earth & Environmental Science [data set], https://doi.org/10.1594/PANGAEA.875196, 2017.

Maturilli, M., Herber, A., and König-Langlo, G.: Climatology and time series of surface meteorology in Ny-Ålesund, Svalbard, Earth Syst. Sci. Data, 5, 155–163, https://doi.org/10.5194/essd-5-155-2013, 2013.

725 Mech, M., Ehrlich, A., Herber, A., Lüpkes, C., Wendisch, M., Becker, S., Boose, Y., Chechin, D., Crewell, S., Dupuy, R., Gourbeyre, C., Hartmann, J., Jäkel, E., Jourdan, O., Kliesch, L.-L., Klingebiel, M., Kulla, B. S., Mioche, G., Moser, M., Risse, N., Ruiz-Donoso, E., Schäfer, M., Stapf, J., and Voigt, C.: MOSAiC-ACA and AFLUX - Arctic airborne campaigns characterizing the exit area of MOSAiC, Sci. Data, 9, 790, https://doi.org/10.1038/s41597-022-01900-7, 2022.

Mewes, D. and Jacobi, C.: Heat transport pathways into the Arctic and their connections to surface air temperatures, Atmos. Chem. Phys., 19, 3927–3937, https://doi.org/10.5194/acp-19-3927-2019, 2019.

Moreno-Ibáñez, M., Laprise, R., and Gachon, P.: Recent advances in polar low research: current knowledge, challenges and future perspectives, Tellus A: Dyn. Meteorol. Oceanogr., 73, 1890 412, https://doi.org/10.1080/16000870.2021.1890412, 2021.

Nash, D., Waliser, D., Guan, B., Ye, H., and Ralph, F. M.: The Role of Atmospheric Rivers in Extratropical and Polar Hydroclimate, J. Geophys. Res.: Atmos., 123, 6804–6821, https://doi.org/10.1029/2017JD028130, 2018.

Neff, W., Compo, G. P., Martin Ralph, F., and Shupe, M. D.: Continental heat anomalies and the extreme melting of the Greenland ice surface in 2012 and 1889: Melting of Greenland in 1889 and 2012, J. Geophys. Res.: Atmos., 119, 6520–6536, https://doi.org/10.1002/2014JD021470, 2014.

Newell, R. E., Newell, N. E., Zhu, Y., and Scott, C.: Tropospheric rivers? - A pilot study, Geophys. Res. Lett., 19, 2401–2404, https://doi.org/10.1029/92GL02916, 1992.

OSI SAF: Global Sea Ice Concentration Climate Data Record v2.0 - Multimission, EUMETSAT SAF on Ocean and Sea Ice [data set], https://doi.org/10.15770/EUM_SAF_OSI_0008, 2017.

Papritz, L. and Spengler, T.: A Lagrangian Climatology of Wintertime Cold Air Outbreaks in the Irminger and Nordic Seas and Their Role in Shaping Air–Sea Heat Fluxes, J. Climate, 30, 2717–2737, https://doi.org/10.1175/JCLI-D-16-0605.1, 2017.

Papritz, L., Aemisegger, F., and Wernli, H.: Sources and Transport Pathways of Precipitating Waters in Cold-Season Deep North Atlantic Cyclones, J. Atmos. Sci., 78, 3349–3368, https://doi.org/10.1175/JAS-D-21-0105.1, 2021.

Pithan, F., Medeiros, B., and Mauritsen, T.: Mixed-phase clouds cause climate model biases in Arctic wintertime temperature inversions, Clim. Dyn., 43, 289–303, https://doi.org/10.1007/s00382-013-1964-9, 2014.

Pithan, F., Svensson, G., Caballero, R., Chechin, D., Cronin, T. W., Ekman, A. M. L., Neggers, R., Shupe, M. D., Solomon, A., Tjernström, M., and Wendisch, M.: Role of air-mass transformations in exchange between the Arctic and mid-latitudes, Nat. Geosci., 11, 805–812, https://doi.org/10.1038/s41561-018-0234-1, 2018.

Radovan, A., Crewell, S., Moster Knudsen, E., and Rinke, A.: Environmental conditions for polar low formation and development over the Nordic Seas: study of January cases based on the Arctic System Reanalysis, Tellus A: Dyn. Meteorol. Oceanogr., 71, 1618 131, https://doi.org/10.1080/16000870.2019.1618131, 2019.

Rantanen, M., Karpechko, A. Y., Lipponen, A., Nordling, K., Hyvärinen, O., Ruosteenoja, K., Vihma, T., and Laaksonen, A.: The Arctic has warmed nearly four times faster than the globe since 1979, Commun. Earth Environ., 3, 168, https://doi.org/10.1038/s43247-022-00498-3, 2022.

Rasmussen, E. A. and Turner, J.: Polar lows: Mesoscale weather systems in the polar regions, Cambridge University Press, 2003.

Rückert, J. E., Rostosky, P., Huntemann, M., Clemens-Sewall, D., Ebell, K., Kaleschke, L., Lemmetyinen, J., Macfarlane, A. R., Naderpour, R., Stroeve, J., Walbröl, A., and Spreen, G.: Sea ice concentration satellite retrievals influenced by surface changes due to warm air intrusions: A case study from the MOSAiC expedition, Elem. Sci. Anth., EarthArXiv [preprint], https://doi.org/10.31223/X5VW85, 2023-03-24, 2023.

Screen, J. A. and Simmonds, I.: The central role of diminishing sea ice in recent Arctic temperature amplification, Nature, 464, 1334–1337, https://doi.org/10.1038/nature09051, 2010.

Serreze, M. C. and Barry, R. G.: Processes and impacts of Arctic amplification: A research synthesis, Global Planet. Change, 77, 85–96, https://doi.org/10.1016/j.gloplacha.2011.03.004, 2011.

Serreze, M. C., Barrett, A. P., Stroeve, J. C., Kindig, D. N., and Holland, M. M.: The emergence of surface-based Arctic amplification, The Cryosphere, 3, 11–19, https://doi.org/10.5194/tc-3-11-2009, 2009.

Shapiro, M. A. and Keyser, D.: Fronts, Jet Streams and the Tropopause, in: Extratropical Cyclones, edited by Newton, C. W. and Holopainen, E. O., pp. 167–191, American Meteorological Society, Boston, MA, https://doi.org/10.1007/978-1-944970-33-8_10, 1990.

770 Shestakova, A. A., Chechin, D. G., Lüpkes, C., Hartmann, J., and Maturilli, M.: The foehn effect during easterly flow over Svalbard, Atmos. Chem. Phys., 22, 1529–1548, https://doi.org/10.5194/acp-22-1529-2022, 2022.

Spreen, G. and Kern, S.: Methods of satellite remote sensing of sea ice, in: Sea Ice, edited by Thomas, D. N., pp. 239–260, John Wiley & Sons, Ltd, Chichester, UK, https://doi.org/10.1002/9781118778371.ch9, 2016.

Spreen, G., Kaleschke, L., and Heygster, G.: Sea ice remote sensing using AMSR-E 89-GHz channels, J. Geophys. Res.: Oceans, 113,
775 C02S03, https://doi.org/10.1029/2005JC003384, 2008.

Sprenger, M. and Wernli, H.: The LAGRANTO Lagrangian analysis tool – version 2.0, Geosci. Model Dev., 8, 2569–2586, https://doi.org/10.5194/gmd-8-2569-2015, 2015.

Stendel, M., Francis, J., White, R., Williams, P. D., and Woollings, T.: The jet stream and climate change, in: Climate Change, pp. 327–357, Elsevier, https://doi.org/10.1016/B978-0-12-821575-3.00015-3, 2021.

780 Stevens, B., Ament, F., Bony, S., Crewell, S., Ewald, F., Gross, S., Hansen, A., Hirsch, L., Jacob, M., Kölling, T., Konow, H., Mayer, B., Wendisch, M., Wirth, M., Wolf, K., Bakan, S., Bauer-Pfundstein, M., Brueck, M., Delanoë, J., Ehrlich, A., Farrell, D., Forde, M., Gödde, F., Grob, H., Hagen, M., Jäkel, E., Jansen, F., Klepp, C., Klingebiel, M., Mech, M., Peters, G., Rapp, M., Wing, A. A., and Zinner, T.: A High-Altitude Long-Range Aircraft Configured as a Cloud Observatory: The NARVAL Expeditions, Bull. Am. Meteorol. Soc., 100, 1061–1077, https://doi.org/10.1175/BAMS-D-18-0198.1, 2019.

785 Stoll, P. J.: A global climatology of polar lows investigated for local differences and wind-shear environments, Weather Clim. Dyn., 3, 483–504, https://doi.org/10.5194/wcd-3-483-2022, 2022.

Stroeve, J., Nandan, V., Willatt, R., Dadic, R., Rostosky, P., Gallagher, M., Mallett, R., Barrett, A., Hendricks, S., Tonboe, R., McCrystall, M., Serreze, M., Thielke, L., Spreen, G., Newman, T., Yackel, J., Ricker, R., Tsamados, M., Macfarlane, A., Hannula, H.-R., and Schneebeli, M.: Rain on snow (ROS) understudied in sea ice remote sensing: a multi-sensor analysis of ROS during MOSAiC (Multidisciplinary drifting Observatory for the Study of Arctic Climate), The Cryosphere, 16, 4223–4250, https://doi.org/10.5194/tc-16-4223-2022, 2022.

790

Terpstra, A., Michel, C., and Spengler, T.: Forward and Reverse Shear Environments during Polar Low Genesis over the Northeast Atlantic, Mon. Weather Rev., 144, 1341–1354, https://doi.org/10.1175/MWR-D-15-0314.1, 2016.

Terpstra, A., Renfrew, I. A., and Sergeev, D. E.: Characteristics of Cold Air Outbreak events and associated Polar Mesoscale Cyclogenesis over the North Atlantic region, J. Climate, pp. 1–52, https://doi.org/10.1175/JCLI-D-20-0595.1, 2021.

795 Tjernström, M., Shupe, M. D., Brooks, I. M., Persson, P. O. G., Prytherch, J., Salisbury, D. J., Sedlar, J., Achtert, P., Brooks, B. J., Johnston, P. E., Sotiropoulou, G., and Wolfe, D.: Warm-air advection, air mass transformation and fog causes rapid ice melt: WARM-AIR ADVECTION, FOG AND ICE MELT, Geophys. Res. Lett., 42, 5594–5602, https://doi.org/10.1002/2015GL064373, 2015.

Viceto, C., Gorodetskaya, I. V., Rinke, A., Maturilli, M., Rocha, A., and Crewell, S.: Atmospheric rivers and associated precipitation patterns during the ACLOUD and PASCAL campaigns near Svalbard (May–June 2017): case studies using observations, reanalyses, and a regional climate model, Atmos. Chem. Phys., 22, 441–463, https://doi.org/10.5194/acp-22-441-2022, 2022.

800

Wahl, S., Bollmeyer, C., Crewell, S., Figura, C., Friederichs, P., Hense, A., Keller, J. D., and Ohlwein, C.: A novel convective-scale regional reanalysis COSMO-REA2: Improving the representation of precipitation, metz, 26, 345–361, https://doi.org/10.1127/metz/2017/0824, 2017.

Wang, C., Graham, R. M., Wang, K., Gerland, S., and Granskog, M. A.: Comparison of ERA5 and ERA-Interim near-surface air tempera-ture, snowfall and precipitation over Arctic sea ice: effects on sea ice thermodynamics and evolution, The Cryosphere, 13, 1661–1679, https://doi.org/10.5194/tc-13-1661-2019, 2019.

Wendisch, M., Macke, A., Ehrlich, A., Lüpkes, C., Mech, M., Chechin, D., Dethloff, K., Velasco, C. B., Bozem, H., Brückner, M., Clemen, H.-C., Crewell, S., Donth, T., Dupuy, R., Ebell, K., Egerer, U., Engelmann, R., Engler, C., Eppers, O., Gehrmann, M., Gong, X., Gottschalk, M., Gourbeyre, C., Griesche, H., Hartmann, J., Hartmann, M., Heinold, B., Herber, A., Herrmann, H., Heygster, G., Hoor, P., Jafariserajehlou, S., Jäkel, E., Järvinen, E., Jourdan, O., Kästner, U., Kecorius, S., Knudsen, E. M., Köllner, F., Kretzschmar, J., Lelli, L., Leroy, D., Maturilli, M., Mei, L., Mertes, S., Mioche, G., Neuber, R., Nicolaus, M., Nomokonova, T., Notholt, J., Palm, M., van Pinx-teren, M., Quaas, J., Richter, P., Ruiz-Donoso, E., Schäfer, M., Schmieder, K., Schnaiter, M., Schneider, J., Schwarzenböck, A., Seifert, P., Shupe, M. D., Siebert, H., Spreen, G., Stapf, J., Stratmann, F., Vogl, T., Welti, A., Wex, H., Wiedensohler, A., Zanatta, M., and Zeppenfeld, S.: The Arctic Cloud Puzzle: Using ACLOUD/PASCAL Multiplatform Observations to Unravel the Role of Clouds and Aerosol Particles in Arctic Amplification, Bull. Am. Meteorol. Soc., 100, 841–871, https://doi.org/10.1175/BAMS-D-18-0072.1, 2019.

Wendisch, M., Handorf, D., Tegen, I., Neggers, R., and Spreen, G.: Glimpsing the Ins and Outs of the Arctic Atmospheric Cauldron, Eos, 102, https://doi.org/10.1029/2021EO155959, 2021.

Wendisch, M., Brückner, M., Crewell, S., Ehrlich, A., Notholt, J., Lüpkes, C., Macke, A., Burrows, J. P., Rinke, A., Quaas, J., Maturilli, M., Schemann, V., Shupe, M. D., Akansu, E. F., Barrientos-Velasco, C., Bärfuss, K., Blechschmidt, A.-M., Block, K., Bougoudis, I., Bozem, H., Böckmann, C., Bracher, A., Bresson, H., Bretschneider, L., Buschmann, M., Chechin, D. G., Chylik, J., Dahlke, S., Deneke, H., Dethloff, K., Donth, T., Dorn, W., Dupuy, R., Ebell, K., Egerer, U., Engelmann, R., Eppers, O., Gerdes, R., Gierens, R., Gorodetskaya, I. V., Gottschalk, M., Griesche, H., Gryanik, V. M., Handorf, D., Harm-Altstädter, B., Hartmann, J., Hartmann, M., Heinold, B., Herber, A., Herrmann, H., Heygster, G., Höschel, I., Hofmann, Z., Hölemann, J., Hünerbein, A., Jafariserajehlou, S., Jäkel, E., Jacobi, C., Janout, M., Jansen, F., Jourdan, O., Jurányi, Z., Kalesse-Los, H., Kanzow, T., Käthner, R., Kliesch, L. L., Klingebiel, M., Knudsen, E. M., Kovács, T., Körtke, W., Krampe, D., Kretzschmar, J., Kreyling, D., Kulla, B., Kunkel, D., Lampert, A., Lauer, M., Lelli, L., von Lerber, A., Linke, O., Löhnert, U., Lonardi, M., Losa, S. N., Losch, M., Maahn, M., Mech, M., Mei, L., Mertes, S., Metzner, E., Mewes, D., Michaelis, J., Mioche, G., Moser, M., Nakoudi, K., Neggers, R., Neuber, R., Nomokonova, T., Oelker, J., Papakonstantinou-Presvelou, I., Pätzold, F., Pefanis, V., Pohl, C., van Pinxteren, M., Radovan, A., Rhein, M., Rex, M., Richter, A., Risse, N., Ritter, C., Rostosky, P., Rozanov, V. V., Donoso, E. R., Saavedra Garfias, P., Salzmann, M., Schacht, J., Schäfer, M., Schneider, J., Schnierstein, N., Seifert, P., Seo, S., Siebert, H., Soppa, M. A., Spreen, G., Stachlewska, I. S., Stapf, J., Stratmann, F., Tegen, I., Viceto, C., Voigt, C., Vountas, M., Walbröl, A., Walter, M., Wehner, B., Wex, H., Willmes, S., Zanatta, M., and Zeppenfeld, S.: Atmospheric and Surface Processes, and Feedback Mechanisms Determining Arctic Amplification: A Review of First Results and Prospects of the (AC)3 Project, Bull. Am. Meteorol. Soc., 104, E208–E242, https://doi.org/10.1175/BAMS-D-21-0218.1, 2023.

Wesche, C., Steinhage, D., and Nixdorf, U.: Polar aircraft Polar5 and Polar6 operated by the Alfred Wegener Institute, JLSRF, 2, A87, https://doi.org/10.17815/jlsrf-2-153, 2016.

Woods, C. and Caballero, R.: The Role of Moist Intrusions in Winter Arctic Warming and Sea Ice Decline, J. Climate, 29, 4473–4485, https://doi.org/10.1175/JCLI-D-15-0773.1, 2016.

Woods, C., Caballero, R., and Svensson, G.: Large-scale circulation associated with moisture intrusions into the Arctic during winter: MOISTURE INTRUSIONS DURING ARCTIC WINTER, Geophys. Res. Lett., 40, 4717–4721, https://doi.org/10.1002/grl.50912, 2013.

You, C., Tjernström, M., Devasthale, A., and Steinfeld, D.: The Role of Atmospheric Blocking in Regulating Arctic Warming, Geophys. Res. Lett., 49, https://doi.org/10.1029/2022GL097899, 2022.

Yu, Y., Xiao, W., Zhang, Z., Cheng, X., Hui, F., and Zhao, J.: Evaluation of 2-m Air Temperature and Surface Temperature from ERA5 and ERA-I Using Buoy Observations in the Arctic during 2010–2020, Remote Sens., 13, 2813, https://doi.org/10.3390/rs13142813, 2021.

Zahn, M. and von Storch, H.: A long-term climatology of North Atlantic polar lows, Geophys. Res. Lett., 35, L22 702, https://doi.org/10.1029/2008GL035769, 2008.

Ziereis, H. and Gläßer, M.: HALO - Global Player für die Atmosphärenforschung, Deutsches Zentrum für Luft- und Raumfahrt (DLR), https://elib.dlr.de/51508/, 2006.

845